Mössbauer Effect Reference and Data Journal

August 2015 • Volume 38 • Number 6

Mössbauer spectroscopic investigation of Fe-based silicides

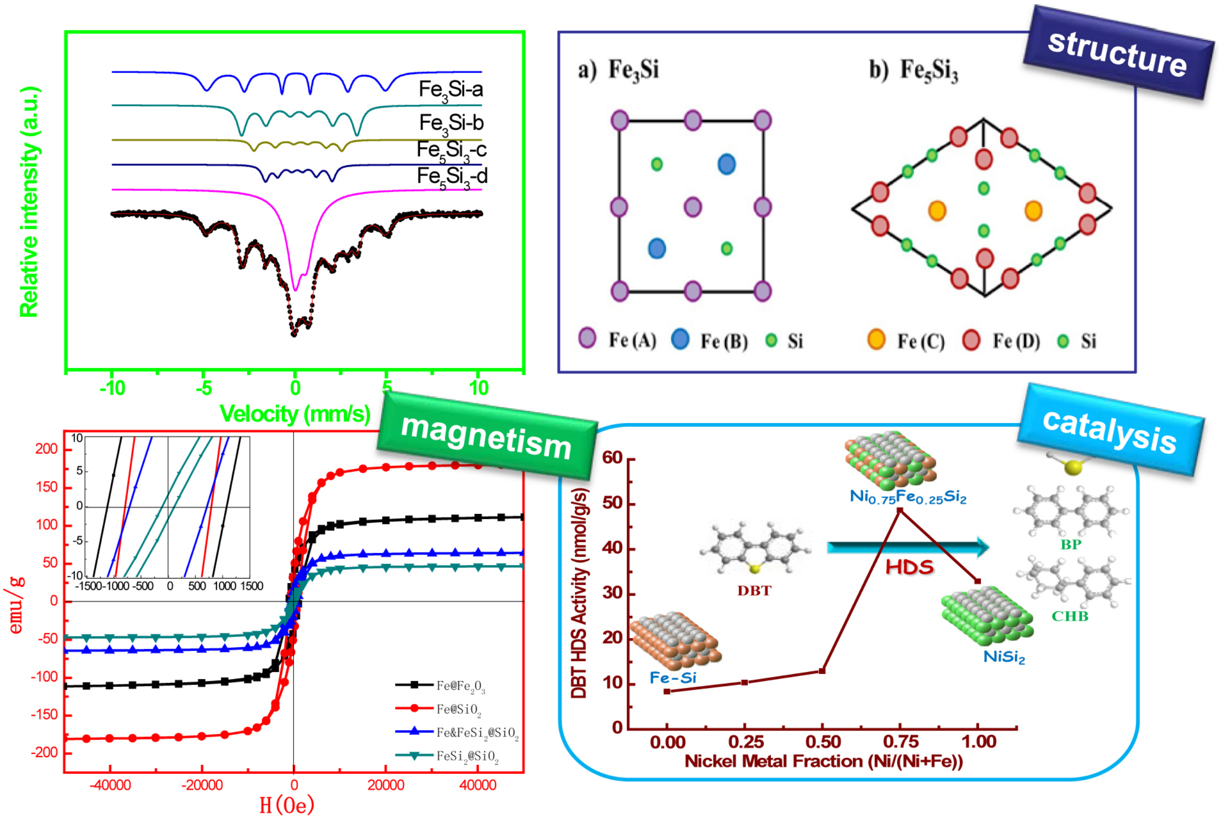

Lab of Advanced Materials & Catalytic Engineering

Dalian University of Technology

MÖSSBAUER SPECTROSCOPY
NEWSLETTER

August 2015

Synthesis and Mössbauer spectroscopic investigation of Fe-based silicides

Xiao Chen[a], Junhu Wang[b], Changhai Liang[a,*]
[a] Laboratory of Advanced Materials and Catalytic Engineering, School of Chemical Engineering, Dalian University of Technology, Dalian 116024, China
[b] Mössbauer Effect Data Center, Dalian Institute of Chemical Physics, Chinese Academy of Sciences, Dalian 116023, China
Email: changhai@dlut.edu.cn

Biography

Xiao Chen received his doctorate degree at Dalian University of Technology in 2013. His doctoral dissertation title was "synthesis, characterization, and hydrogenation properties of transition metal silicide catalysts". He has won several competitive awards, including the academic doctoral prize by the Ministry of Education and the 8th China youth science and technology innovation award. He is currently a lecturer of chemical technology, working in the lab of advanced materials & catalytic engineering at Dalian University of Technology. His main research area at present is intermetallic compounds in catalysis.

Junhu Wang got his doctorate degree at Toho University in Japan in 2002. He became a full professor in 2008 at Dalian Institute of Chemical Physics, Chinese Academy of Sciences, and he has been granted the outstanding scholarship foundation of CAS (100 Talents Program) for the applications of in-situ catalysis Mössbauer technique. He started his Mössbauer study since 1996. His doctoral thesis focused on Mössbauer spectroscopic studies on the structural chemistry of gadolinium, erbium and neptunium compounds. His main research area at present includes "development and application of novel catalytic and adsorption materials" and "in-situ Mössbauer characterization".

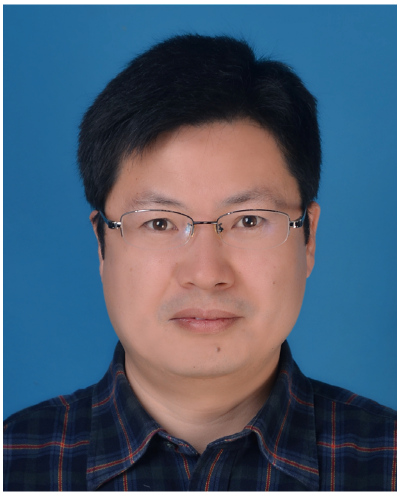

Changhai Liang is a professor in the School of Chemical Engineering at Dalian University of Technology, China. He earned his doctorate degree in physical chemistry from Dalian Institute of Chemical Physics, Chinese Academy of Sciences in 2000. He successively became an assistant professor and associated professor at the Dalian Institute of Chemical Physics in 2001 and 2003, respectively. He then spent about 3 years at the Ruhr University of Bochum, Germany, and ETH in Zurich, Switzerland, as the Alexander von Humboldt Research Fellow and postdoctoral fellow. He joined the School of Chemical Engineering at Dalian University of Technology in 2006 and was promoted as a full professor. His research interests include controlled synthesis of new catalytic materials and catalytic reaction kinetics for energy conversion, environmental protection, and fine chemicals synthesis.

Abstract

Mössbauer spectroscopic investigation on bulk and supported iron-based silicides was reviewed. The bulk and supported iron-based silicides were synthesized by using various methods, such as mechanical alloying, pyrolysis of silicon-containing metallic precursor, and temperature programmed silicification. The information of phases, structure, and particle sizes of iron-based silicides have been identified by Mössbauer spectroscopy. Due to the dissolution of Si atoms into the iron lattice, the structure of particles changed from cubic iron to iron silicides (cubic B20 FeSi, cubic DO_3 Fe_3Si, hexagonal Fe_5Si_3, and orthorhombic $FeSi_2$). Mössbauer spectroscopy was also a good tool to reveal the magnetic properties of iron-based silicides. ^{57}Fe Mössbauer spectra, M-H curves and FC and ZFC curves demonstrated that the as-prepared Fe_3Si nanoparticles presented superparamagnetic behavior at room temperature and ferromagnetic behavior at low temperature. Especially, the reduced particle size had a great impact on the magnetic properties of the as-prepared nanoparticles, including saturation magnetizations, Curie temperatures and blocking temperatures. In addition, ^{57}Fe Mössbauer spectroscopic results also provided strong evidence the relationship between the structure of iron silicides and catalytic properties. In $Ni_{1-x}Fe_xSi_2$ catalysts, Fe atoms with higher *d*-electron counts substituted Ni atoms, which distorted the six rings in the structure. The DBT activity for the $Ni_{1-x}Fe_xSi_2$ has the following order: $Ni_{0.75}Fe_{0.25}Si_2 > NiSi_2 > Ni_{0.50}Fe_{0.50}Si_2 \approx Ni_{0.25}Fe_{0.75}Si_2 \approx$ Fe-Si. The positive synergistic effect on HDS activity can be correlated to the formation of Ni-Fe and Fe-Si bonds, which may enhance the π adsorption of DBT, promoting the hydrogenation activity.

1. Introduction

Transition metal silicides represent a rich variety of refractory materials [1, 2], and have specific crystal and electronic structures different from those of their component metals due to the strong interaction between metals and silicon [3]. Transition metal silicides have received much attention because of their unique physical and chemical properties, such as high thermal stability, low electrical resistivity, low work function, and low density [4]. Such metal silicide materials could meet the requirements of modern technological applications, including nanoelectronics [5, 6], field emitters [7], spintronics [8], thermoelectric [9, 10], solar energy conversion [11]. Meanwhile, in recent years, active research is being done on metal silicides usable as hydrogenation and hydrodesulfurization catalysts [12-19]. Especially iron silicide can be used as a potential candidate material in new silicon-compatible devices for photovoltaic [20] and spintronic [21] applications and the Kondo insulator FeSi, the semiconductor β-$FeSi_2$, and the metallic compound α-$FeSi_2$ have been found among them.

Due to the effect of electronegativity, atomic size, and electron density, the crystal structure of transition metal silicides present great difference, including cubic (C1, $L1_2$, DO_3, B20), hexagonal, tetragonal, and complex construction. For example, the Fe_3Si crystallizes in the DO_3 structure, which composed by two sublattices in unit cell. One of sublattice contained 8 Fe atoms, and another sublattice contained 4 Fe atoms and 4 Si atoms, which occupied the cube vertices alternately, as shown in Figure 1. However, the FeSi crystallizes in the B20 structure, which formed by the simple cubic structure composed by Fe atoms and Si atoms, respectively.

General and rational chemical synthesis of silicide nanomaterials is challenging, due in part to the multiple stoichiometries and complex phase behavior exhibited by many silicide compounds. For instance, there are six known iron silicide intermetallic compounds (Fe_3Si, Fe_2Si, Fe_5Si_3, FeSi, a-$FeSi_2$, and b-$FeSi_2$) only three of which are stable at room temperature (Figure 2) [22]. In such complicated materials systems careful control and characterize over

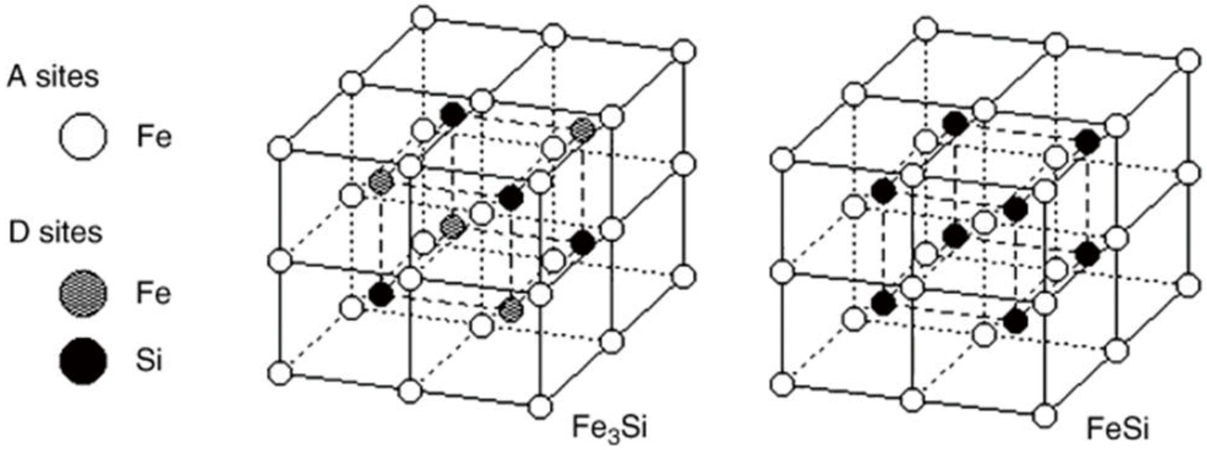

Figure 1. Unit cells of Fe_3Si with the DO_3 structure and FeSi with the B20 structure.

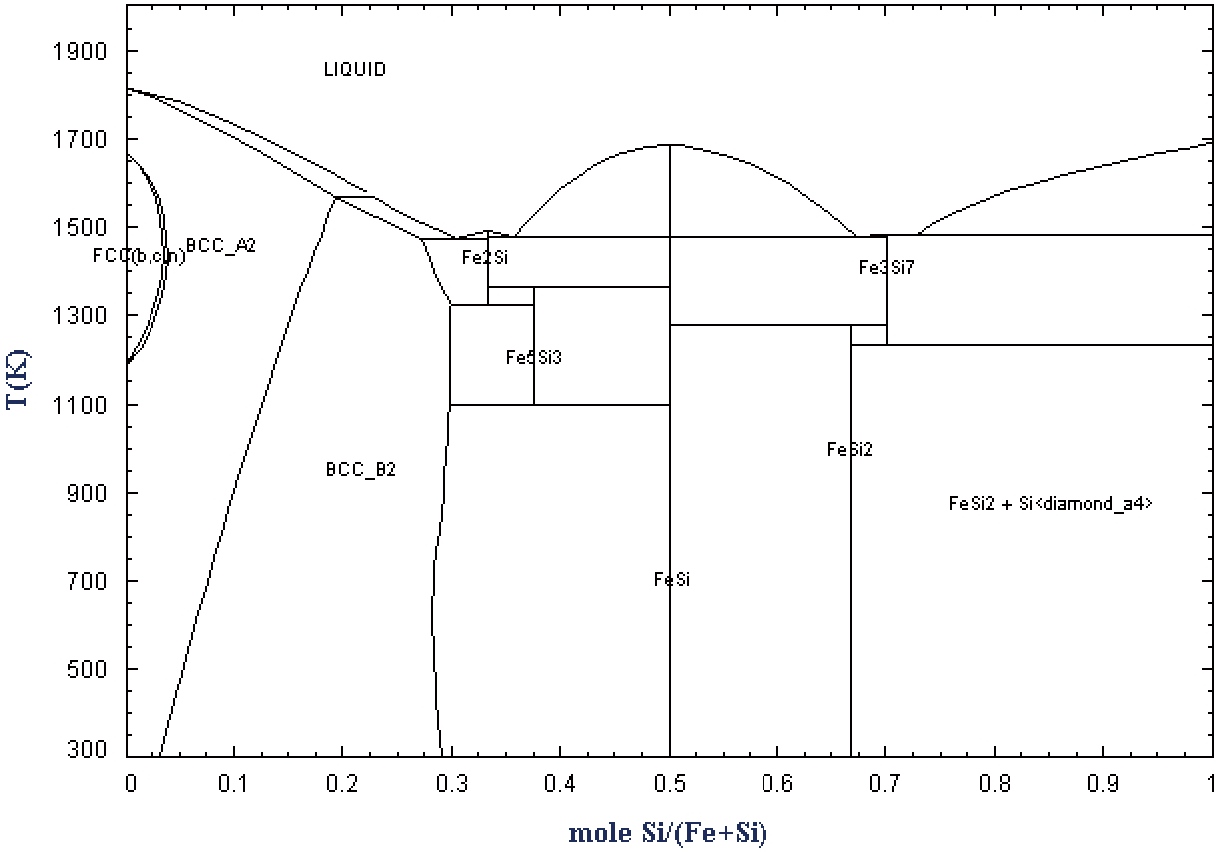

Figure 2. Fe-Si binary phase diagram (reprinted from SGTE binary alloy databases) [22].

synthesized phases can be quite difficult. In the recently year, multiple chemical methods have been developed for generating iron silicide nanostructures with controlled size or phase, such as chemical vapor transport [23, 24], chemical vapor deposition [12, 25], wet chemistry method [26] and direct silane silicification method [27] for nanowires or nanoparticles.

In addition, ^{57}Fe Mössbauer spectroscopy is a well-known tool for clarifying the chemical state and relative amount of the iron species [28]. Aiming to characterize many kinds of iron-bearing environmental and chemical state during the formation of iron silicides, our group studied the structure of iron silicides by Mössbauer spectroscopy. ^{57}Fe Mössbauer spectra were recorded at room temperature using a Topologic 500 A spectrometer with a proportional counter. Moving ^{57}Co(Rh) in a constant acceleration mode was used as the radioactive source. All of the spectral analyses were conducted assuming a Lorentzian lineshape for computer folding and fitting. The Doppler velocity of the spectrometer was calibrated with respect to α-Fe foil. And the free recoil fraction was assumed to be the same for all iron species. In this way, Mössbauer parameters such as the isomer shift (IS), the electric quadrupole splitting (QS), the full linewidth at half maximum (LW), the magnetic hyperfine field (H), and the relative resonance areas of the different components of the absorption patterns (RI) were determined.

In our previous research, multiple ways to synthesis the iron-based silicides have been developed, including mechanical alloying, pyrolysis of silicon-containing metallic precursor [29, 30], and temperature programmed silicification [31-33]. The composition and structure of iron-based silicides has been studied by ^{57}Fe Mössbauer spectroscopy in detail. ^{57}Fe Mössbauer spectroscopic results provided strong evidence the relationship between the structure and magnetic/catalytic properties.

2. Rapid preparation of Fe_3Si-Al_2O_3 nanocomposite by mechanical alloying and heat treatment

2.1. Synthesis of Fe_3Si-Al_2O_3 nanocomposite

Commercial Fe_3O_4, Al, and Si powders as raw materials were milled in a QM-3SP04 planetary ball mill (Nanjing, China). The ball-to-powder mass ratio was 30:1, and the rotation speed was 500 r/min in the mechanical alloying process, as shown in Figure 3. Fe_3O_4, Al, and Si powders with their molar ratios of 3:8:3, 3:8:4.5 and 3:8:9 were milled for a certain time and then annealed at 900 °C for 1 h in H_2, which were respectively designated as 1Si-xh-900, 1.5Si-xh-900 and 3Si-xh-900. The reaction is shown in the Eqn. (1) below:

$$3Fe_3O_4 + 3Si + 8Al \rightarrow 3Fe_3Si + 4Al_2O_3 \quad (1)$$

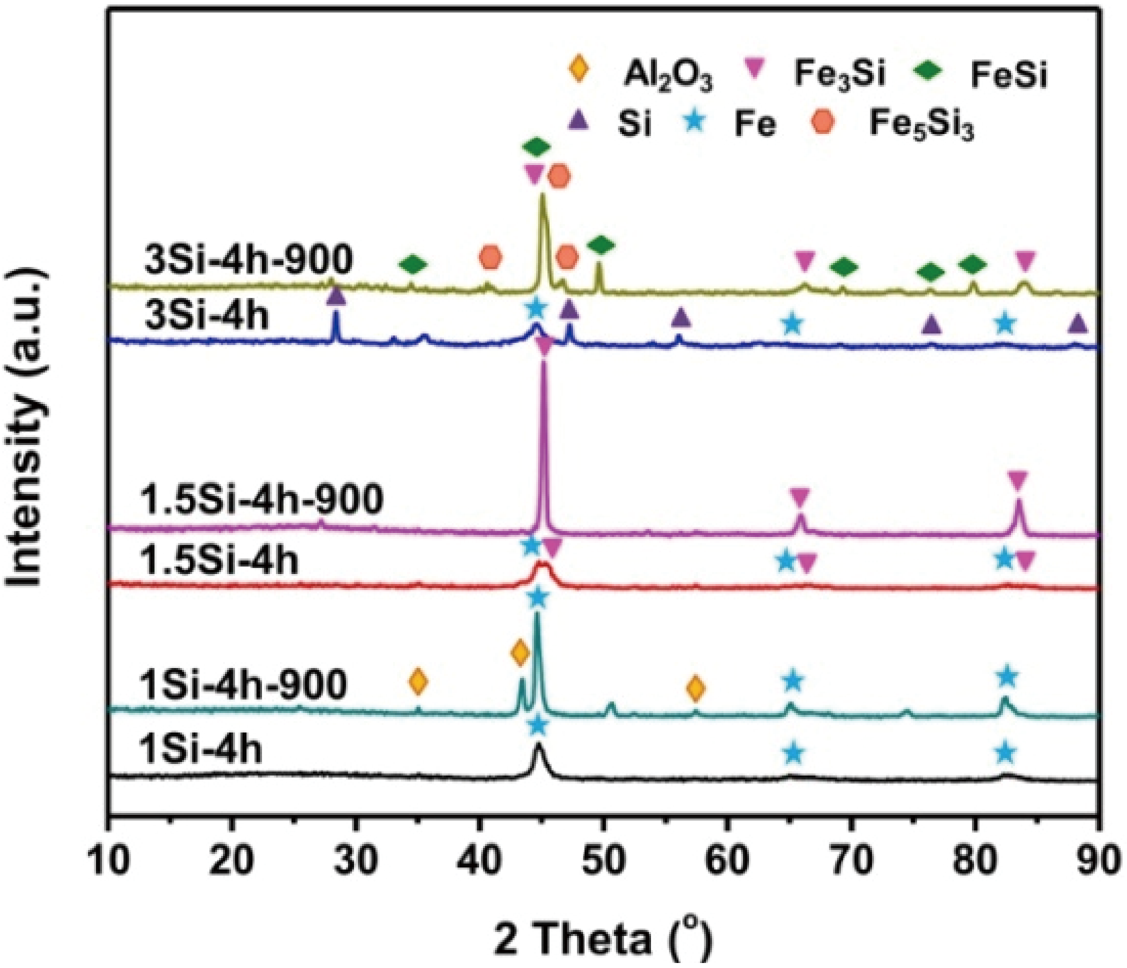

Figure 3. Powder XRD patterns of the samples obtained after ball-milling and annealing at 900 °C for 1 h in H_2.

Powder XRD patterns of the samples obtained after ball-milling and annealing at 900 °C for 1 h in H_2 are shown in Figure 3. From the above analysis, the crystalline phase of the samples milled for 4 h transformed from Fe to a mixture of Fe_3Si and Fe with the proportion of Si in raw materials increasing. For sample 3Si-4h, diffraction peaks at 28.4°, 47.3°, 56.1°, 76.4° and 88.1° were attributed to Si (111), (220), (311), (331) and (422) (PDF No. 27-1402), respectively. Although the proportion of Si in raw materials further increased, no Fe_3Si or other iron silicide was generated. Similar to the dilution effect of $CaCl_2$ reported by D. Restrepo et al. [34], the addition of excess Si might decrease the particle sizes of Fe and Si and consequently facilitate the formation of Fe_3Si. However, seriously excess Si could not be grinded to sufficiently fine particles under a fixed output of the ball mill in our experiments, which made it hard to produce Fe_3Si. In order to promote the complete reaction between Fe and Si, the samples milled for 4 h were further annealed at 900 °C for 1 h in H_2. For sample 1Si-4h-900, the intensity of diffraction peaks indexed to Fe and Al_2O_3 became much stronger, indicating that the obtained Fe-Al_2O_3 nanocomposite had better crystalline form and larger particle size after high temperature treatment. For sample 1.5Si-4h-900, only Fe_3Si was observed, which revealed that unreacted Fe in sample 1.5Si-4h all transformed to Fe_3Si under 900 °C in H_2. For sample 3Si-4h-900, diffraction peaks at 40.8°, 41.3°, 45.3°, 46.6° and 47.1° were due to Fe_5Si_3 (210), (102), (211), (300) and (112) (PDF No. 89-2047), and diffraction peaks at 34.6°, 45.1°, 49.7°, 69.4°, 76.5° and 80.0° were indexed to FeSi (111), (210), (211), (311), (320) and (321) (PDF No. 38-1397). In addition, the phase Fe_3Si also existed in sample 3Si-4h-900. Because of obviously excess Si, unreacted Fe in sample 3Si-4h transformed to a mixture of Fe_3Si, Fe_5Si_3 and FeSi under 900 °C in H_2. Especially, no Al_2O_3 was observed in samples 1.5Si-4h-900 and 3Si-4h-900, since good crystalline form of Al_2O_3 might be influenced by excess Si under high temperature treatment.

2.2 Mössbauer spectra of Fe_3Si-Al_2O_3 nanocomposite

^{57}Fe Mössbauer spectra of the as-prepared samples measured at room temperature are shown in Figure 4 and corresponding Mössbauer parameters are listed in Table 1. The Mössbauer

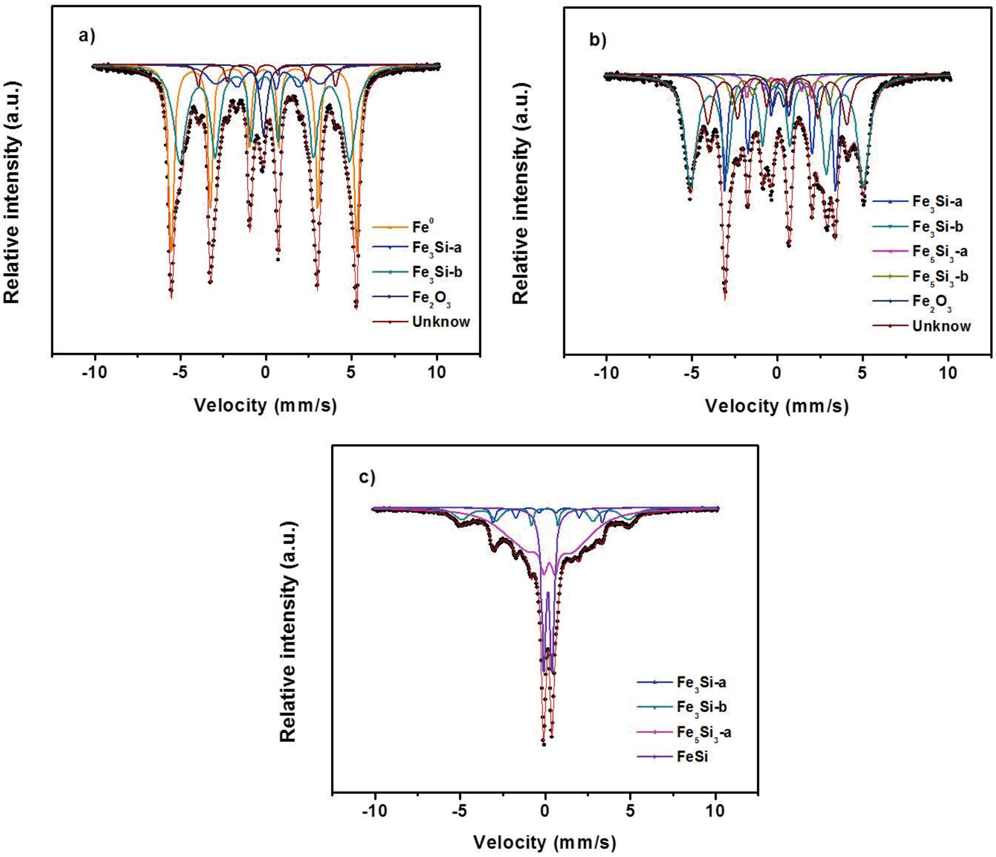

Figure 4. ^{57}Fe Mössbauer spectra of samples (a) 1Si-4h-900, (b) 1.5Si-4h-900, and (c) 3Si-4h-900.

spectrum of sample 1Si-4h-900 could be fitted into four sextets and a doublet. One sextet with IS = -0.11 mm/s and H = 33.8 T was indexed to Fe^0, which accounted for 36.3%. The two sextets with IS = 0.12 mm/s, H = 19.1 T and IS = -0.08 mm/s, QS = 0.02 mm/s, H = 30.9 T were respectively assigned to the Fe atoms at nonequivalent lattice sites A and B of Fe_3Si with the cubic DO_3 structure [30, 32, 35]. However, no diffraction peaks due to Fe_3Si were observed in the XRD pattern of sample 1Si-4h-900, which indicated that Fe_3Si might exist in an amorphous state. The doublet with IS = -0.14 mm/s and QS = 0 mm/s can probably be identified as amorphous metallic iron, which accounted for 4.3%. The Mössbauer spectrum of sample 1.5Si-4h-900 was composed of five sextets. Except two sextets corresponding to Fe_3Si, the other two sextets with IS = 0.18 mm/s, H = 17.6 T and IS = 0.21 mm/s, QS = -0.19 mm/s, H = 11.9 T were respectively indexed to the two types of Fe atoms in Fe_5Si_3 [30, 36], which accounted for 11.5%. Similarly, above Fe_5Si_3 might be amorphous, because no diffraction peaks due to Fe_5Si_3 were observed in the XRD pattern of sample 1.5Si-4h-900. The Mössbauer spectrum of sample 3Si-4h-900 could be fitted into three sextets and a doublet. The doublet with IS = 0.15 mm/s, QS = 0.48 mm/s was assigned to FeSi [32, 37], which accounted for 24.4%. Besides, Fe_3Si and Fe_5Si_3 also existed in sample 3Si-4h-900. Especially for samples 1Si-4h-900 and 1.5Si-4h-900, the sextet with IS = 0.06 (0.08) mm/s, H = 25.0 (25.2) T had not obtained a reasonable attribution and needed further confirmation. In a word, ^{57}Fe Mössbauer spectra revealed the existence of amorphous phases Fe_3Si and Fe_5Si_3, which effectively supplemented XRD result.

3. Iron silicide on silica prepared by pyrolysis of ferrocene-polydimethylsilane composites

3.1. Synthesis and Mössbauer spectra of iron silicide on silica

Iron silicides nanoparticles with a size of about 6-9 nm well dispersed on silica have been prepared by pyrolysis of ferrocene-polydimethylsilane composites. Typically, a certain amount of ferrocene and 1.0 g of polydimethylsilane (PDMS) ($m_{ferrocene} : m_{PDMS}$ = 3:1, 3:2, 1:1, 2:3 and 1:3) in 150 mL of tetrahydrofuran were stirred for 12 h. Orange powder ($Fe(Si(CH_3)_2R)_2$) was obtained after rotary evaporation and vacuum drying. The obtained composites were respectively heated to 600 °C, 700 °C and 800 °C at a rate of 10 °C min^{-1} in Ar, and then maintained at these temperatures for 120 min. The black solids resulted from thermolysis of the composite

Table 1. ^{57}Fe Mössbauer parameters of samples 1Si-4h-900, 1.5Si-4h-900 and 3Si-4h-900.

Sample	Assignment	IS/mm/s	QS/mm/s	H/T	RI/%	LW/mm/s
1Si-4h-900	Fe^0	-0.11	-	33.8	36.3	0.28
	Fe_3Si-a	0.12	-	19.1	11.1	0.34
	Fe_3Si-b	-0.08	0.02	30.9	44.7	0.39
	Fe_2O_3	0.14	-	-	4.3	0.46
	Unknow	0.06	-	25.0	3.6	0.22
1.5Si-4h-900	Fe_3Si-a	0.15	-	20.2	24.7	0.34
	Fe_3Si-b	-0.05	0.04	31.4	48.0	0.44
	Fe_5Si_3-c	0.18	-	17.6	7.4	0.46
	Fe_5Si_3-d	0.21	-0.19	11.9	4.1	0.33
	Unknow	0.08	-0.01	25.2	15.8	0.31
3Si-4h-900	Fe_3Si-a	0.14	0.01	20.0	4.7	0.29
	Fe_3Si-b	-0.02	0.03	30.5	12.6	0.22
	Fe_5Si_3-d	0.19	-0.10	12.6	58.3	0.53
	FeSi	0.15	0.48	-	24.4	0.30

Isomer shift (IS) is referred to arufa-Fe foil at room temperature. Uncertainty is ±5% of the reported value.

with mass ratio of ferrocene and PDMS 1:1 at different temperatures were respectively designated as Ar-600, Ar-700 and Ar-800.

In order to reveal the particle distribution and crystalline structure, the as-prepared samples were investigated by TEM measurements, as shown in Figure 5a-c. It revealed that iron silicide nanoparticles were highly dispersed and uniformly deposited on amorphous silica support. And statistics of about 100 nanoparticles for each sample suggested that average particle sizes of the samples Ar-600, Ar-700 and Ar-800 were respectively 7.6 nm, 12.6 nm and 16.2 nm with corresponding standard deviations of ±1.5 nm, ±2.1 nm and ±2.2 nm. Corresponding size histograms of iron silicide nanoparticles are listed in Figure 5g-i. By comparing the three samples, it was found that the particle sizes increased with increasing the pyrolysis temperature due to the aggregation effect under higher temperatures. The representative high-resolution TEM images are shown in Figure 5d-f and corresponding FFT patterns are shown in the insets. For the sample Ar-600, the measured lattice spacing of the particle was 0.201 nm, which was in good accordance with the (220) plane of Fe_3Si (JCPDS PDF45-1207). The same phase Fe_3Si was also observed in the sample Ar-700. For the sample Ar-800, the measured lattice spacing was 0.194 nm, matching well with the (112) plane of Fe_5Si_3 (JCPDS PDF89-2047). It was concluded that highly dispersed iron silicide (Fe_3Si and Fe_5Si_3) nanoparticles on silica had been prepared by pyrolysis of ferrocene-polydimethylsilane composites.

^{57}Fe Mössbauer spectra of the samples Ar-600, Ar-700 and Ar-800 measured at room temperature are shown in Figure 6. And the Mössbauer parameters are listed in Table 2. The Mössbauer spectrum of the sample Ar-600 could be fitted into two sextets and an asymmetric doublet. The two sextets with IS = 0.21 mm/s, H = 19.8 T and IS = 0.06 mm/s, H = 31.2 T were attributed to the Fe atoms on nonequivalent lattice sites A and B of Fe_3Si

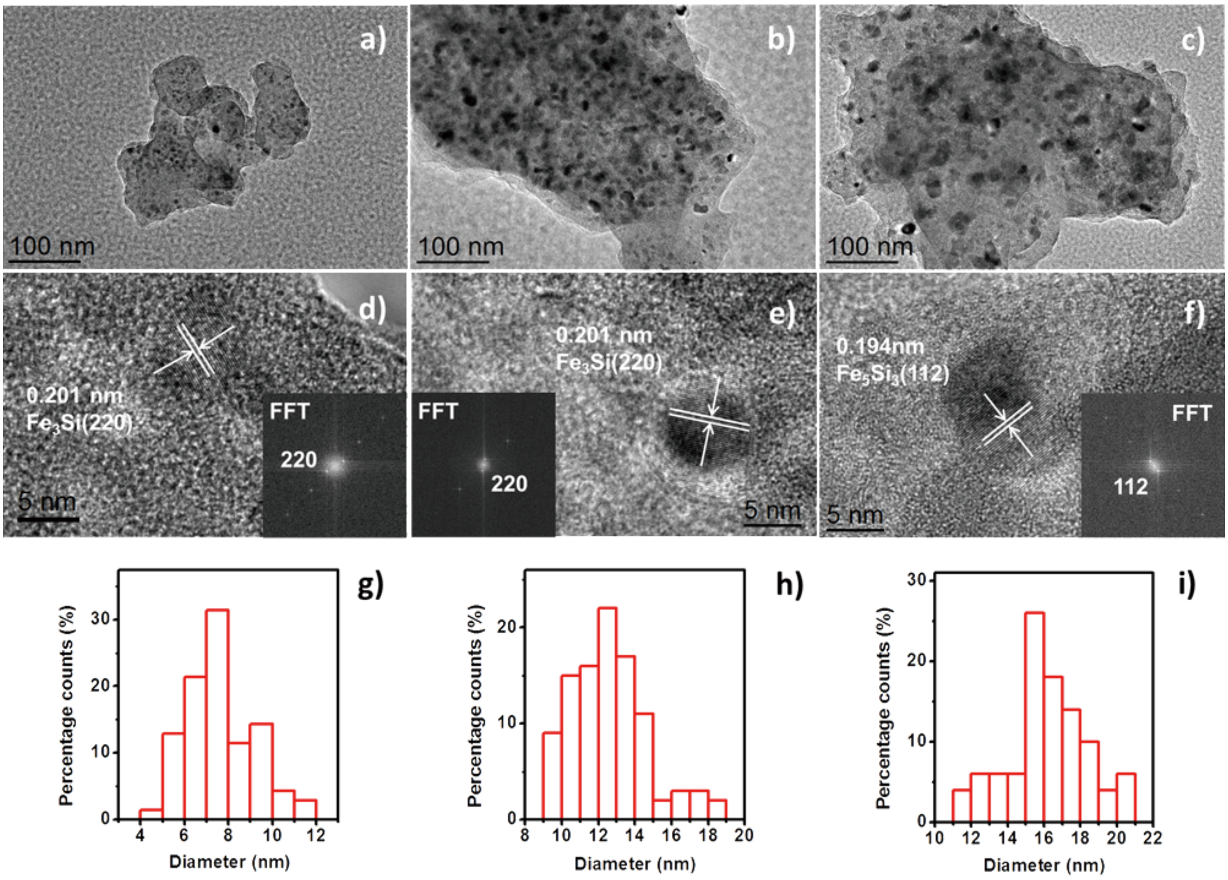

Figure 5. Representative TEM and high-resolution TEM images of the samples (a, d) Ar-600, (b, e) Ar-700, and (c, f) Ar-800. (Insets: FFT patterns of the corresponding particles) (g-i) size histograms of iron silicide nanoparticles in the corresponding samples.

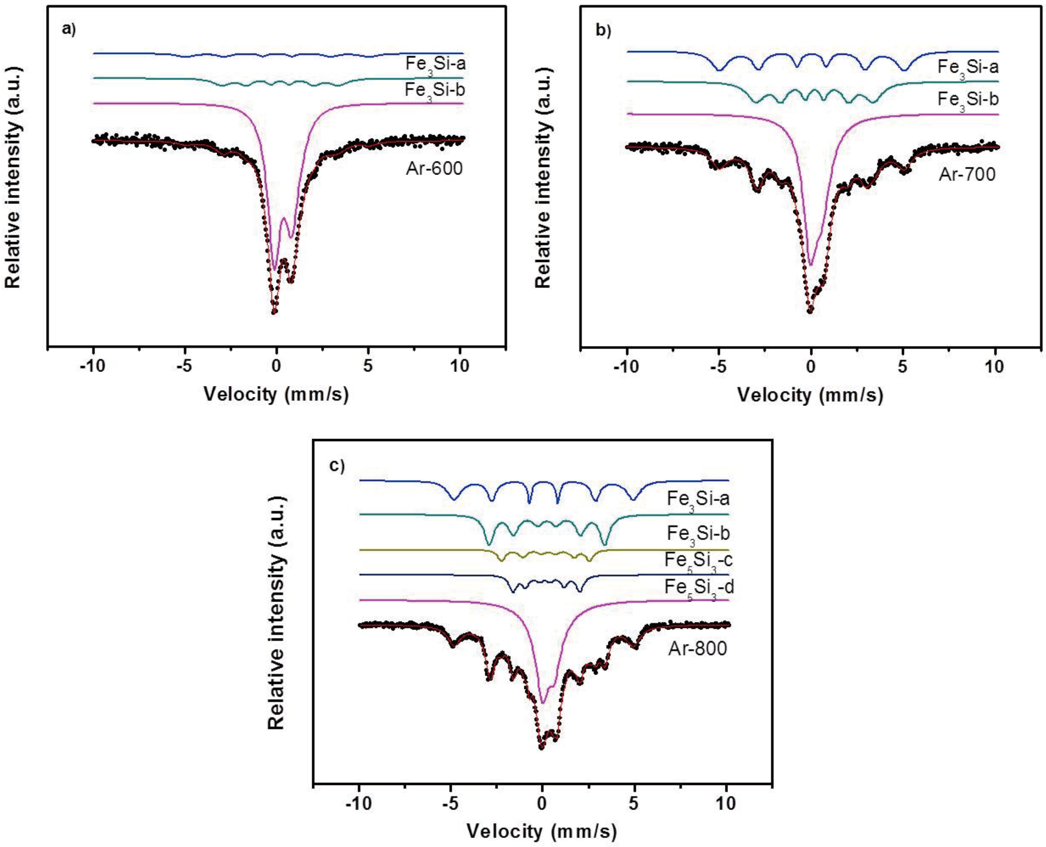

Figure 6. ^{57}Fe Mössbauer spectra of the samples (a) Ar-600, (b) Ar-700, and (c) Ar-800.

Table 2. ^{57}Fe Mössbauer parameters of the samples Ar-600, Ar-700 and Ar-800.

Sample	Assignment	IS/mm/s	QS/mm/s	H/T	RI/%	LW/mm/s
Ar-600	Fe_3Si-a	0.21	-	19.8	11.7	0.50
	Fe_3Si-b	0.06	-	31.2	5.2	0.43
	magnetic relaxation	0.35	-	5.0	83.1	0.53
Ar-700	Fe_3Si-a	0.21	-	19.8	24.6	0.50
	Fe_3Si-b	0.06	-	31.2	21.5	0.43
	magnetic relaxation	0.27	-	6.3	53.9	0.74
Ar-800	Fe_3Si-a	0.25	-	19.6	21.5	0.65
	Fe_3Si-b	0.07	-	30.3	19.3	0.24
	Fe_5Si_3-c	0.24	-0.16	14.9	6.1	0.47
	Fe_5Si_3-d	0.17	0.09	11.3	9.2	0.47
	magnetic relaxation	0.29	-	15.0	43.8	0.38

Isomer shift (IS) is refered to arufa-Fe foil at room temperature. Uncertainty is ±5% of the reported value.

with the cubic DO_3 structure, respectively [32, 35]. As shown in Figure 7a, Fe atoms on sites B have eight nearest-neighbor Fe atoms, while Fe atoms on sites A have four nearest-neighbor Fe atoms and four Si atoms. The asymmetric doublet was speculated to be the magnetically relaxed subspectrum arising from low-size Fe_3Si particles, which accounted for 83.1% [38]. Similarly, for the sample Ar-700, the Mössbauer spectrum was fitted into two sextets for Fe_3Si and an asymmetric doublet for its magnetic relaxation. And the percentage of low-size Fe_3Si particles in the sample Ar-700 decreased to 53.9% because of partial particles aggregating with the temperature increasing. The Mössbauer spectrum of the sample Ar-800 was composed of four sextets and an asymmetric doublet. The two sextets with IS = 0.25 mm/s, H = 19.6 T and IS = 0.07 mm/s, H = 30.3 T were assigned to Fe_3Si, while the other two sextets with IS = 0.24 mm/s, QS = -0.16 mm/s, H = 14.9 T and IS = 0.17 mm/s, QS = 0.09 mm/s, H = 11.3 T were assigned to the two types of Fe atoms in Fe_5Si_3, respectively. Figure 7b illustrates its projection onto the basal plane.34 The Mössbauer parameters of Fe_5Si_3 obtained here were a bit different from those reported in the literature [36, 39], which were not consistent either and further confirmation is needed. And the percentage of low-size Fe_3Si (and Fe_5Si_3) particles in the sample Ar-800 sequentially decreased to 43.8%. On the other hand, ^{57}Fe Mössbauer spectra indicated that all the three samples displayed superparamagnetic behavior at room temperature due to small sizes of Fe_3Si (and Fe_5Si_3) nanoparticles.

3.2. Magnetic properties of iron silicide on silica

So as to understand the magnetic properties of the samples, M-H curves were measured at 27 °C. Figure 8a revealed that all the three samples exhibited paramagnetic behavior at 27 °C. And the samples were all almost saturated at the magnetic field of 10 kOe. The saturation magnetizations (9.9 emu/g at 27 °C) of the sample Ar-600 (small Fe_3Si nanoparticles on silica) were much lower than those (21.1 emu/g at 27 °C) of the sample Ar-700 (large Fe_3Si nanoparticles on silica), which was attributed to obvious decrease of the Fe_3Si nanoparticle size in the sample Ar-600 [40]. Meanwhile the saturation magnetizations (20.1 emu/g at 27 °C) of the sample Ar-800 (large Fe_3Si and Fe_5Si_3 nanoparticles on silica) were slightly lower than those of the sample Ar-700, which might result from the lower saturation magnetization of Fe_5Si_3 than that of Fe_3Si. The saturation magnetization value of Fe_5Si_3 was uncertain since few reports had been published about it, while the saturation magnetization value of Fe_3Si thin film was reported to be 590 emu/cm^3 (82.0 emu/g) [41]. It was rational that saturation magnetizations of all the three samples were much lower than 82.0 emu/g because of the reduced particle sizes and a diamagnetic contribution from the silica support.

FC and ZFC curves were measured for the three samples to further reveal their magnetic properties. As shown in Figure 8b, the intersections of FC and ZFC curves manifested that Curie temperature (T_C) of the sample Ar-600

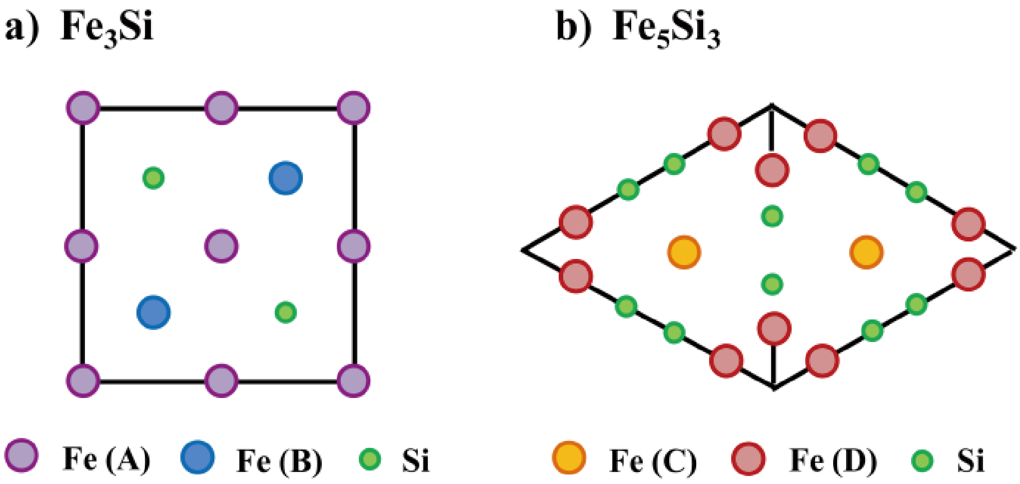

Figure 7. The structures of (a) Fe_3Si and (b) Fe_5Si_3 projected onto the basal plane.

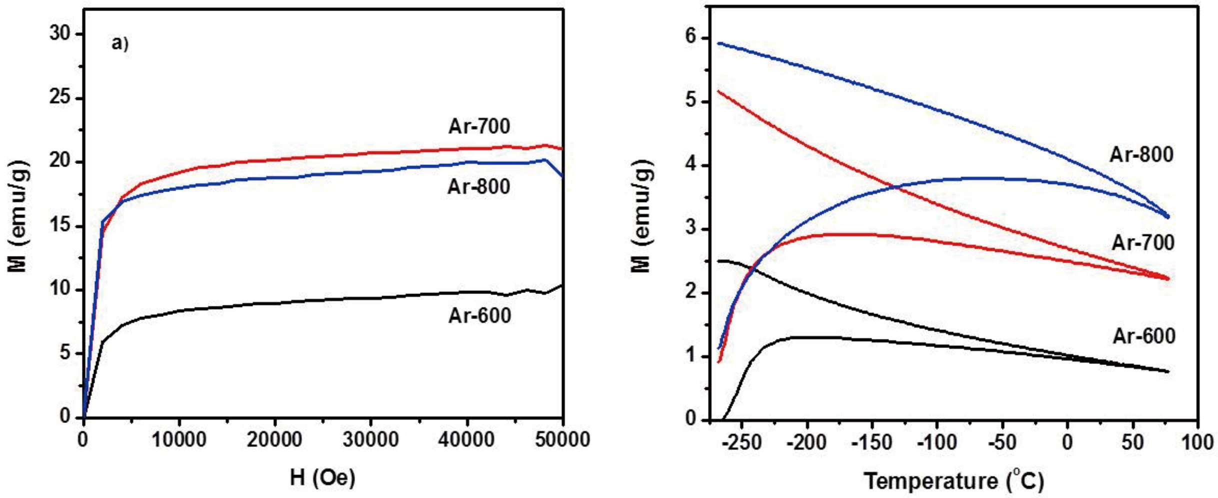

Figure 8. The M-H curves (a) and the FC and ZFC curves (b) of the samples Ar-600, Ar-700 and Ar-800.

was about 27 °C and Curie temperatures of the samples Ar-700 and Ar-800 were both close to 77 °C and even above 77 °C. It had been reported that Curie temperature of Fe_3Si was 530 °C [42]. The Curie temperatures of the samples Ar-600 and Ar-700 decreasing was supposed to be a consequence of the reduced Fe_3Si nanoparticle size [43]. Curie temperature of Fe_5Si_3 was reported to be 112 °C [44]. In addition, the ZFC curves indicated that blocking temperatures of the samples Ar-600, Ar-700 and Ar-800 were -193 °C, -168 °C and -63 °C, respectively. In other words, the as-prepared iron silicide (Fe_3Si and Fe_5Si_3) nanoparticles would exhibit superparamagnetic behavior above the blocking temperatures. In summary, all the three samples presented superparamagnetic behavior at 27 °C. Especially, the reduced nanoparticle sizes had great impacts on the magnetic properties of the samples, such as saturation magnetizations, Curie temperatures, and blocking temperatures.

4. Synthesis and phase transition of iron silicides by temperature programmed silicification

4.1. Synthesis and Mössbauer spectra of iron silicide-silica core-shell structure

$Fe@SiO_2$ and $FeSi_2@SiO_2$ nanoparticles with core-shell structure can be synthesized by temperature programmed silicification of Fe_2O_3 nanoparticles, using silane as silicon source. Fe_2O_3 nanoparticles were reduced at 400 °C in flowing hydrogen (30 mL/min) for 3 h in a quartz microreactor and then underwent silicification at various temperatures (350 °C, 450 °C, 550 °C) for 15 min in a 110 mL/min SiH_4/H_2 mixture ($V_{SiH4:H2}$ = 1:10). To avoid the further oxidation, the samples were passivated in 1% O_2/Ar overnight. The obtained solids were designated as $Fe@SiO_2$, $Fe\&FeSi_2@SiO_2$, $FeSi_2@SiO_2$, respectively.

Figure 9 shows XRD patterns of samples prepared at different conditions. For the $Fe@SiO_2$ sample, diffraction peaks at $2\theta = 44.67^\circ$, 65.02° and 82.33° can be found, which are assigned to Fe (110), (200), and (211) (JCPDS 06-0696), respectively. With increasing silicification temperature, a mixture of phases was formed in the $Fe\&FeSi_2@SiO_2$ sample. Small diffraction peaks at about 29.06° and 49.44° corresponding to the $FeSi_2$ (JCPDS 20-0532) appeared, while the peaks corresponding to Fe (200) and Fe (211) became weaker and stronger, respectively. When the silicification temperature increased to 550 °C, the $FeSi_2@SiO_2$ sample was formed. The diffraction peaks belonging to $FeSi_2$ became stronger and the peaks belonging to Fe almost vanished completely except for a very weak Fe (110) signal. These results suggest that the Si atoms were deposited on the Fe surface and then diffused into the crystal lattice of iron atom to form $FeSi_2$. Interestingly, the peaks of Fe_2O_3 and SiO_2 cannot be found in the silicified samples upon exposure to the air. A similar phenomenon was observed previously in the literature for the SiO_2-coated Fe sample [45]. This suggests that the SiO_2 may be amorphous, and exists on the surface as a shell that protects the metallic Fe and $FeSi_2$ from oxidation. However, for the $Fe@Fe_2O_3$ sample prepared without the silicification, peaks at 35.7° and 83° belonging to Fe_2O_3 (119) and (4, 0, 12) (JCPDS 25-1402), respectively, can be detected in addition to those corresponding to bcc-Fe. The formation of Fe_2O_3

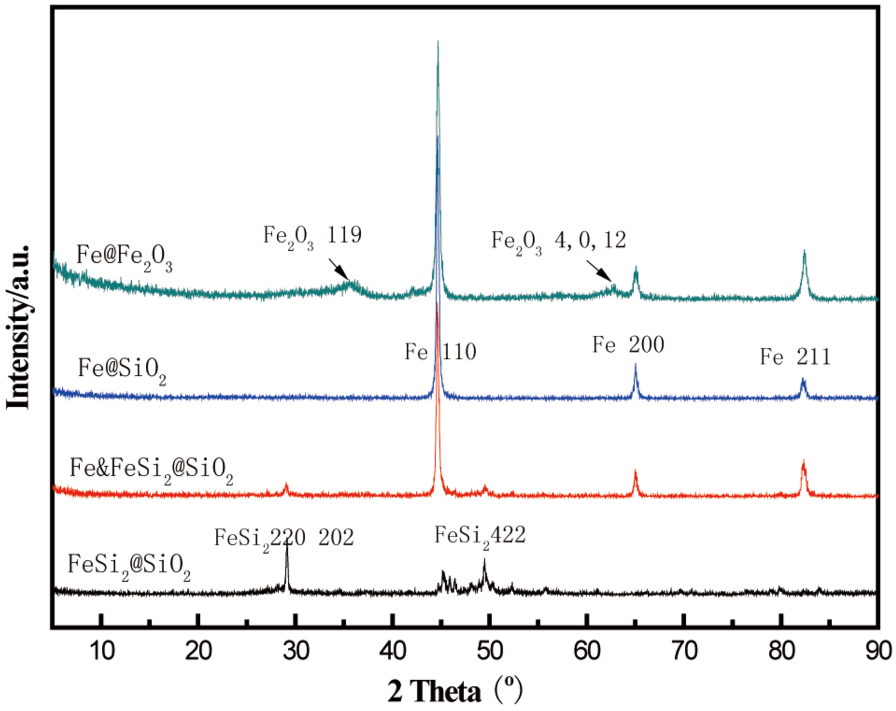

Figure 9. XRD patterns of $Fe@Fe_2O_3$, $Fe@SiO_2$, $Fe\&FeSi_2@SiO_2$, and $FeSi_2@SiO_2$ samples.

was due to the outer layer of the iron particle reacting with the O_2 when exposed to air. $FeSi_2$ is formed by the reaction between iron and Si, according to following reaction pathways in the Eqn. (2-3) below:

$$Fe(s) + Si(s) \longrightarrow FeSi_2(s) \quad (2)$$

$$Fe(s) + SiH_4(g) \longrightarrow FeSi_2(s) + H_2(g) \quad (3)$$

In order to determine the chemical state and coordination of the iron species in the samples, ^{57}Fe Mössbauer spectra were measured at room temperature. The results were shown in Figure 10, with the hyperfine interaction parameters summarized in Table 3. The Mössbauer spectrum of $Fe@Fe_2O_3$ (Figure 10a) could be fitted into a Fe^{3+} doublet and a sextuplet for Fe^0. The IS value is considered the most important Mössbauer parameter that is influenced by the chemical state of iron [46]. The obtained ^{57}Fe Mössbauer parameters of IS = 0.39 mm/s and QS = 0.88 mm/s could be attributed to Fe^{3+}, which is in good agreement with typical reported Fe^{3+} IS values that are less than 0.4 $mm{\cdot}s^{-1}$ [47]. This doublet accounted for about 38% of the total spectral area; the sextuplet with IS = 0 and QS = 0 could be attributed to Fe^0, which accounted for the remaining 62% of the total spectral area.

The Mössbauer spectrum of $Fe@SiO_2$ is shown in Figure 10b. There was only a sextuplet for Fe^0, with no other spectrum being detected, indicating that there was only one chemical state for iron. For the $Fe\&FeSi_2@SiO_2$ sample, the Mössbauer spectrum (Figure 10c) could be fitted with a doublet and a sextuplet. The sextuplet associated with Fe^0 accounted for 66% of the total spectral area, while the doublet having ^{57}Fe Mössbauer parameters of IS = 0.14 mm/s and QS = 0.47 mm/s accounted for about 34% and is attributed to $FeSi_2$ [48]. When the silicification temperature was raised to 550 °C to form $FeSi_2@SiO_2$, the Mössbauer spectrum (Figure 10d) could also be fitted into a doublet and a sextuplet. The sextuplet could again be ascribed to Fe^0, while the doublet with the ^{57}Fe Mössbauer parameters of IS = 0.12 mm/s and QS = 0.44 mm/s are attributed to $FeSi_2$ [48]. Compared to the 450 °C silicification temperature, the $FeSi_2@SiO_2$ had a stronger $FeSi_2$ intensity (79%) and a weaker Fe^0 intensity (21%). The structures of the core changed from cubic Fe to orthorhombic $FeSi_2$ with increasing silicification temperature, due to the dissolution of Si atoms into the iron lattices. Interestingly, the Fe_2O_3 phase was not detected by ^{57}Fe Mössbauer spectrum in the samples with silicification compared with the $Fe@Fe_2O_3$. This is attributed to the shell of SiO_2 protecting the core metallic Fe and $FeSi_2$ from oxidation when exposed to air, similar to the XRD patterns (cf. Figure 9).

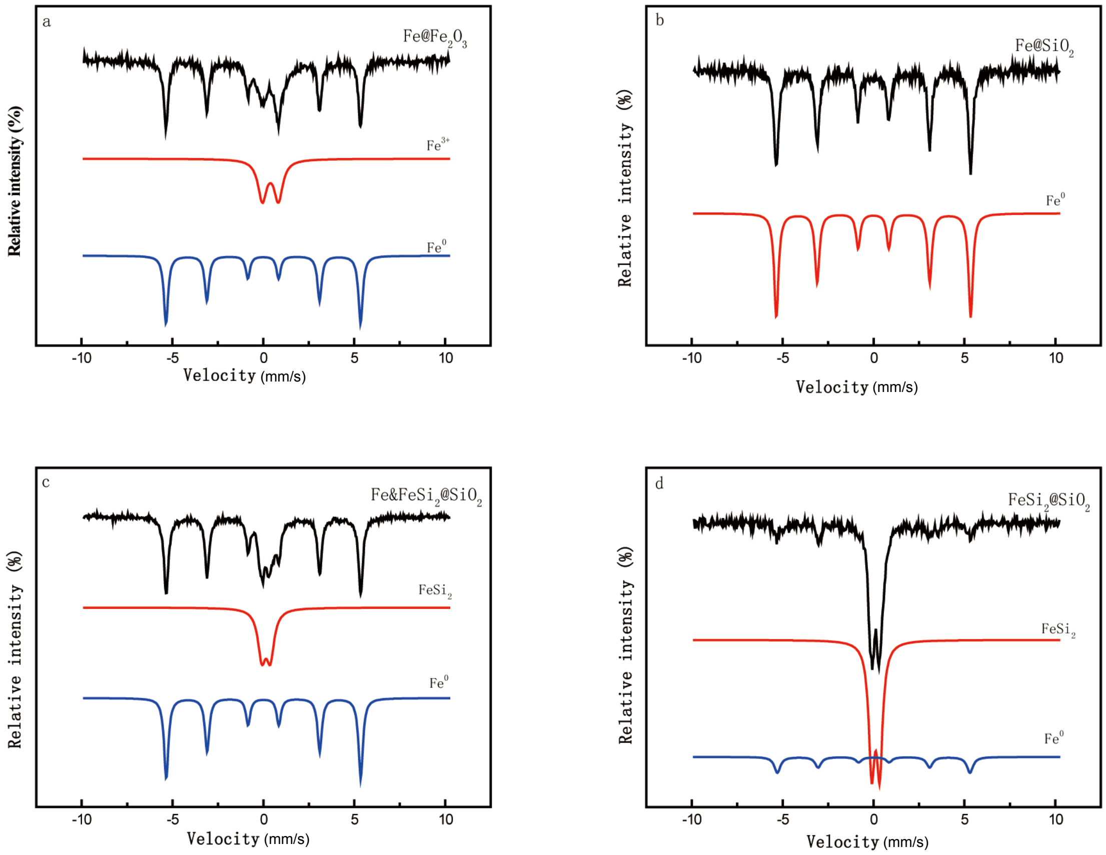

Figure 10. Mössbauer spectra of Fe@Fe$_2$O$_3$ (a), Fe@SiO$_2$ (b), Fe&FeSi$_2$@SiO$_2$ (c), and FeSi$_2$@SiO$_2$ (d).

Table 3. ^{57}Fe Mössbauer parameters of Fe@ Fe$_2$O$_3$, Fe@SiO$_2$, Fe&FeSi$_2$@SiO$_2$, and FeSi$_2$@SiO$_2$ samples.

Sample	state	IS (mm/s)	QS (mm/s)	H (T)	RI (%)	LW (mm/s)
Fe@Fe$_2$O$_3$	Fe^{3+}	0.39	0.88		38	0.58
	Fe^0	0	0	33.2	62	0.28
Fe@SiO$_2$	Fe^0	0	0	33.2	100	0.29
Fe&FeSi$_2$@SiO$_2$	FeSi$_2$	0.14	0.47		34	0.52
	Fe^0	0	0	33.2	66	0.29
FeSi$_2$@SiO$_2$	FeSi$_2$	0.12	0.44		79	0.40
	Fe^0	0.01	-0.01	32.9	21	0.40

4.2. Magnetic properties of silicide-silica core-shell nanoparticles

Magnetic properties of the core-shell nanoparticles were studied by using a commercial superconducting quantum interference device (SQUID) magnetometer. Figure 11 shows the hysteresis loops measured at -268 °C and 27 °C, respectively, and all curves show non-zero coercivities and romance magnetizations, provide a ferromagnetic signature. All four samples were almost saturated at a magnetic field of 20 kOe. The saturation magnetizations (Ms), residual magnetizations (Mr) and coercive force (Hc) decreased with increasing silicification temperature. Compared with the uncoated iron (Ms 221.71 ± 0.08 emu/g) [49], the saturation magnetization of the Fe@SiO$_2$ (180.50 emu/g at -268 °C and 173.93 emu/g at 27 °C) nanoparticles obviously decreased because the diamagnetic contribution of the silica shell resulted in a low mass fraction of the magnetic substance. FeSi$_2$ nanowires were found to have ferromagnetic behavior measured at -271 °C and at room temperature [50], the saturation magnetization values (measured at -268 °C) are positive and quite small [51]. The Cr-doped β-$FeSi_2$ and Ni-doped β-$FeSi_2$ single crystals were also reported to have quite small saturation magnetizations (below 0.02 emu/g) at different temperatures, and provide a ferromagnetic signature at low temperatures [52]. However, intrinsic β-$FeSi_2$ was reported non-magnetic [53], and ferromagnetism was found only at temperatures below -173 °C [54]. The ferromagnetism with certain saturation magnetization (46.72 emu/g at -268 °C and 45.03 emu/g at 27 °C) for $FeSi_2$@SiO_2 was probably attributed to the contribution of the small fraction of Fe in the $FeSi_2$@SiO_2 sample. Thus, with increasing $FeSi_2$ content, and corresponding decrease in Fe content, the saturation magnetizations decreased.

4.3. Thermally induced phase transition of iron silicides

In order to confirm the crystal structure transformation after annealing at high temperature in Ar atmosphere, ^{57}Fe Mössbauer spectra were measured at room temperature as shown in Figure 12. The Mössbauer parameters are listed in Table 4. The Mössbauer spectrum of Fe@$FeSi_2$ (Figure 12a) could be fitted into two doublets and a sextet. The doublet with IS = 0.29 mm/s and QS = 0.44 mm/s could be attributed to α-$FeSi_2$, and the doublet accounted for 15.5% of the total spectral area. The doublet (IS = 0.10 mm/s, QS = 0.42 mm/s) could be attributed to β-$FeSi_2$, which is in good agreement with the literature [55], and accounted for 52% of the total spectral area. The α-structure is developed from the β-structure by the formation of Fe vacancies [56]. The sextet with IS = -0.01 mm/s, QS = -0.01 mm/s and H = 33 T is attributed to Fe^0, which accounted for the remaining 32.5% of the total spectral area.

For the Ar-600 °C-2 h sample (Figure 12b), the Mössbauer spectrum could be well fitted into two doublets and two sextets. The doublet with IS = 0.27 mm/s and QS = 0.50 mm/s could be assigned to FeSi [37], which accounted for about 27% of the total spectral area, while the doublet with IS = 0.08 mm/s and QS = 0.43 mm/s could be attributed to β-$FeSi_2$ [55, 56], which accounted for 26% of the total spectral area.

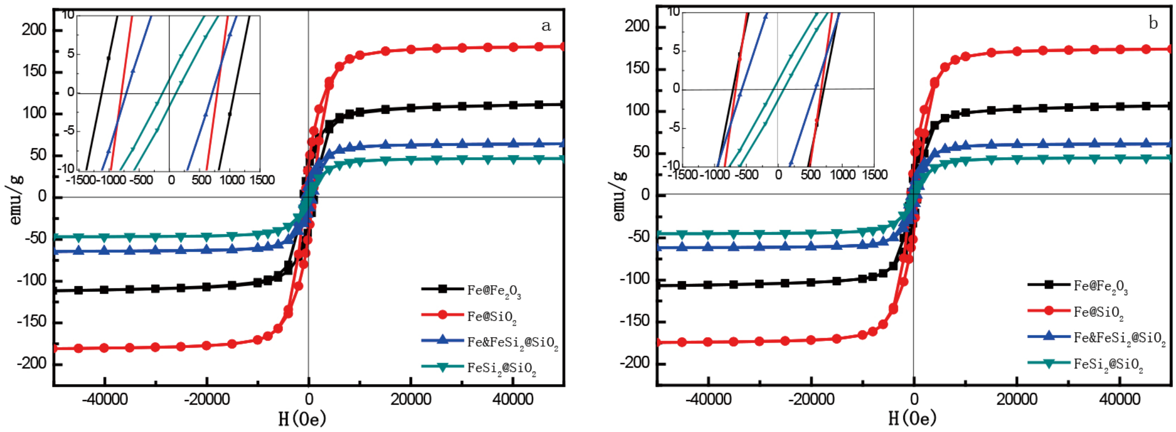

Figure 11. The magnetization curves of Fe@Fe_2O_3, Fe@SiO_2, Fe&$FeSi_2$@SiO_2 and $FeSi_2$@SiO_2 measured at -268 °C (a) and 27 °C (b)

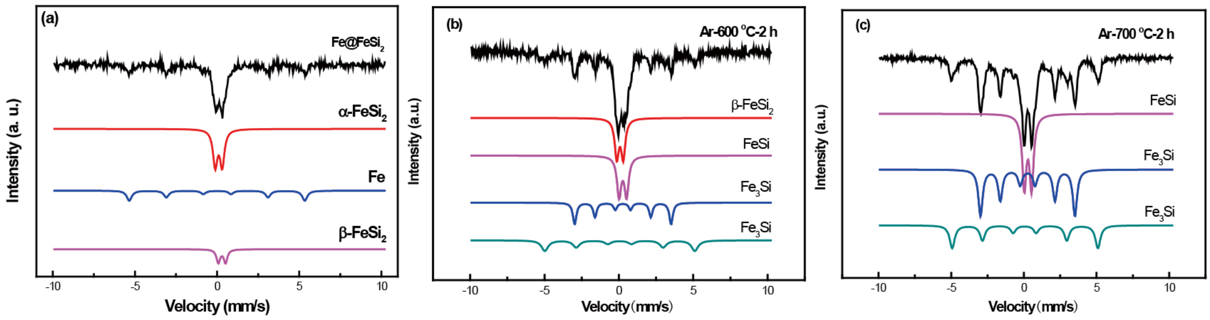

Figure 12. ^{57}Fe Mössbauer spectra of Fe@$FeSi_2$ (a), Ar-600 °C-2 h (b), and Ar-700 °C-2 h (c) samples.

Table 4. ^{57}Fe Mössbauer parameters of Fe@FeSi$_2$, Ar-600 °C-2 h, and Ar-700 °C-2 h samples.

Sample	Phase	IS (mm/s)	QS (mm/s)	H (T)	RI (%)	LW (mm/s)
Fe@FeSi$_2$	β-FeSi$_2$	0.10	0.42	-	52	0.32
	Fe^0	0.36	-0.01	33	32.5	0.37
	α-FeSi$_2$	0.29	0.44		15.5	0.26
Ar-600 °C-2 h	β-FeSi$_2$	0.08	0.43	-	26	0.33
	FeSi	0.27	0.50	-	27	0.34
	Fe$_3$Si-a	0.27	0	20	24	0.28
	Fe$_3$Si-b	0.06	0.01	31	23	0.54
Ar-700 °C-2 h	FeSi	0.28	0.50	-	32	0.34
	Fe$_3$Si-a	0.27	0.01	20	43	0.35
	Fe$_3$Si-b	0.07	0.03	31	25	0.42

The Fe$_3$Si with DO$_3$ structure has two kinds of iron crystallographic sites, which can be well distinguished by Mössbauer spectroscopy [35, 57]. The two sextets with IS = 0.27 mm/s, QS = 0 mm/s, H = 20 T and IS = 0.06 mm/s, QS = 0.01 mm/s, H = 31 T could be attributed to the two kinds of Fe atoms in Fe$_3$Si, respectively. These are consistent with those reported in the literature for bulk Fe$_3$Si alloy [35, 58].

When the annealing temperature was increased to 700 °C, the Mössbauer spectrum (Figure 12c) could be fitted into a doublet and two sextets. The doublet with IS = 0.28 mm/s and QS = 0.50 mm/s could again be ascribed to FeSi [37], which accounted for 32% of the total spectral area. Similar to the Ar-600 °C-2h sample, the two sextets with IS = 0.27 mm/s, QS = 0 mm/s, H = 20 T and IS = 0.07 mm/s, QS = 0.01 mm/s, H = 31 T, could also be attributed to the two types of Fe atoms in Fe$_3$Si, respectively [35, 58]. Compared with Fe@FeSi$_2$, it is interesting to note that FeSi and Fe$_3$Si formed after annealing the sample at 600 °C, and the content of FeSi$_2$ decreased from 69% to 26%, and there was no Fe^0 detected from the Mössbauer spectrum. The Mössbauer results were in good agreement with the XRD result.

A brief schematic for the crystal transformation after thermal annealing is shown in Figure 13. The mechanism of this process can be attributed to the diffusion of Fe and Si in opposite directions. Apparently, during thermal annealing, Si atoms (from the decomposition of SiH$_4$) that were deposited on the surface of the particles diffused inward, and reacted with Fe forming Fe$_3$Si and FeSi. It has been reported that FeSi is the first silicide phase among the possible iron silicides due to its favorable ΔGv, and Fe$_3$Si phase is then generated subsequent to FeSi [59, 60]. The possible reaction pathways have been proposed as follows in the Eqn. (4-6) below:

$$\mathrm{Fe+FeSi_2 \rightarrow 2FeSi} \tag{4}$$
$$\mathrm{5Fe+FeSi_2 \rightarrow 2Fe_3Si} \tag{5}$$
$$\mathrm{FeSi+2Fe \rightarrow Fe_3Si} \tag{6}$$

FeSi and Fe$_3$Si formed while Fe and FeSi$_2$ disappeared when annealing the Fe@FeSi$_2$ sample (not exposed to the air before annealing) at 700 °C for 2 h in Ar atmosphere, which is due

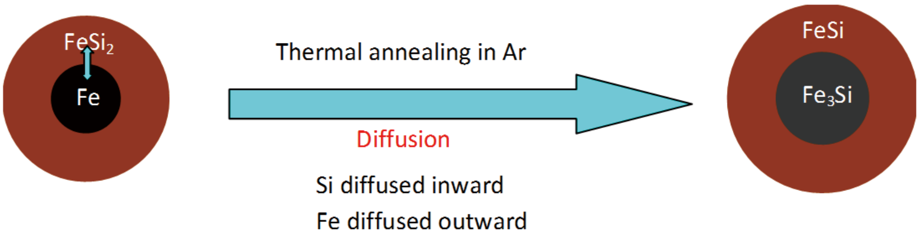

Figure 13. Schematic illustration of the crystal transformation after annealing Fe@FeSi$_2$ sample in Ar atmosphere.

to the thermal interdiffusion of Fe and Si atoms. At higher temperature, the Si diffusion into the bulk Fe is dominant and therefore the content of Si on the surface decreased, while that in the core increased. This phenomenon is similar with the CVD of silicon and silicides on iron [61].

5. Synthesis of Fe substituted Ni-Si intermetallic catalysts by temperature programmed silicification

5.1. Solid-state structural chemistry of Fe substituted Ni-Si intermetallic catalysts

Fe substituted Ni-Si intermetallics with different stoichiometric proportion can be prepared by the temperature programmed silicification of the corresponding oxides. Figure 14 shows the XRD patterns of Fe substituted Ni-Si intermetallics. After the silicification at 450 °C, it clearly shows that the diffraction peaks at 28.6°, 47.4°, 56.3°, 69.3°, 76.6°, and 88.4° reflect the $NiSi_2$ phase (JCPDS 43-0989). However, the phase of iron silicide is not formed, only the zero-valent iron and magnetite Fe_3O_4 phases can be found, comparing with the standard patterns (Fe, JCPD 06-0696, Fe_3O_4, JCPD 19-0629). The formation of Fe_3O_4 is attributed to the oxidation of zero-valent iron when exposed in the air. When a few of Fe dopes into the Ni-Si intermetallic, excepting the $NiSi_2$ phase in the sample of $Ni_{0.75}Fe_{0.25}Si_2$, the diffraction peaks at 44.3°,51.5°, and 75.9° also appear, indicating the formation of Ni-Fe alloy ($FeNi_3$, awaruite, JCPD 38-0419). In addition, by comparison with the ICSD file (FeSi, fersilicite, JCPD 38-1397), those peaks at 45.1°, 49.7°, and 79.9° are attributed to the FeSi lattice planes (210), (211), and (321), respectively. This means the present of Ni promote the formation of iron silicide due to the catalytic of Ni in decomposition of SiH_4 [33]. When the Ni:Fe molar ratio reaches 1:1, the intensity of peaks of $NiSi_2$ and FeSi decrease significantly but the positons of the XRD peaks assigned to $FeNi_3$ phase shifted to lower diffraction angle. Meanwhile, some new peaks at 43.6°, 50.8°, and 74.7° appear, which act in accordance with the standard pattern (JCPD 47-1405), meaning the formation of $Fe_{0.46}Ni_{0.36}$. Further increasing the content of Fe to Ni:Fe molar ratio of 1:3, the phase of $NiSi_2$ and FeSi are disappeared. The main peaks are attributed to the phase of γ-Fe_2O_3 (maghemite-Q, JCPD 25-1402). The relatively weak peak at 44.6° can be attributed to NiFe (kamacite, JCPD 37-0474). Therefore, in the Fe substituted Ni-Si intermetallics, the doping Fe bond with Ni preferentially to form the Ni-Fe alloys. Zero-valent iron is hardly silicified than metallic

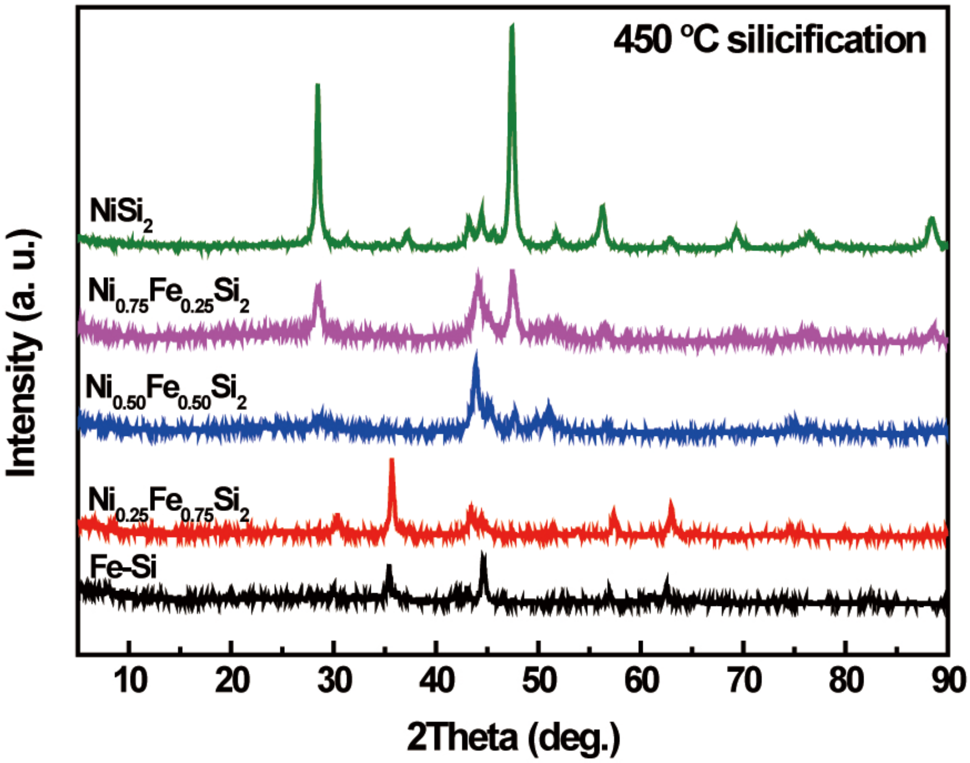

Figure 14. XRD patterns of Fe substituted Ni-Si intermetallics.

nickel due to the higher free energy, however, the present of metallic Ni can promote the reaction of SiH_4 with iron. Due to the formation of the cubic phases of $NiSi_2$ and FeSi and the deviation of ionic radius of Ni^{2+} (0.069 nm) and Fe^{2+} (0.078 nm), the Fe substituting Ni in the Ni-Si intermetallic may influence the metal-silicon and metal-metal interactions, leading to a strong modification of the geometry and electronic structure [62].

^{57}Fe Mössbauer spectroscopy is a well known tool for clarifying the chemical state and relative amount of the iron species. For the catalysts, Mössbauer spectroscopy can get the following information, including identification of phases, determination of oxidation states, structure information, determination of particle size, and kinetics of bulk transformations.

Room temperature ^{57}Fe Mössbauer spectra of samples of $Ni_{0.75}Fe_{0.25}Si_2$, $Ni_{0.50}Fe_{0.50}Si_2$, $Ni_{0.25}Fe_{0.75}Si_2$, and Fe-Si are shown in Figure 15. The related hyperfine interaction parameters are summarized in Table 5. In the Mössbauer spectrum of $Ni_{0.75}Fe_{0.25}Si_2$, one resolved doublet, one singlet, and one sextuplet can be easily identified. The IS value is considered the most important Mössbauer parameter that is influenced by the chemical state of iron. The doublet having ^{57}Fe Mössbauer parameters of IS = 0.27 mm/s, QS = 0.43 mm/s accounted for about 56.4% and is attributed to FeSi [63] ,while the sextuplet with IS = 0.02 mm/s, QS = 0.05 mm/s, and H = 27.3 T could be attributed to $FeNi_3$ [64], which accounted for 33.1% of the total spectral area. The single with the IS = −0.03 mm/s can be ascribed to cubic silicide like $FeSi_2$, which accounted for 10.5% [65]. The cubic structure can be expected because of zero quadrupole splitting which indicates spherical symmetry in the surroundings of the iron atoms. The theoretical calculations based on electron transport model confirmed the structure of nickel silicide changed when Fe atoms with higher *d*-electron counts substituted Ni atoms, which distorted the six rings in the structure and is traced to the formation of Ni-Fe bonds [62]. Therefore, Fe atoms occupy the relative sites in the $Ni_{0.75}Fe_{0.25}Si_2$ material, which preferentially bond with Ni to form alloy and combine with Si to form silicide.

Similarly, for the sample $Ni_{0.50}Fe_{0.50}Si_2$, the Mössbauer spectrum is fitted into two doublet

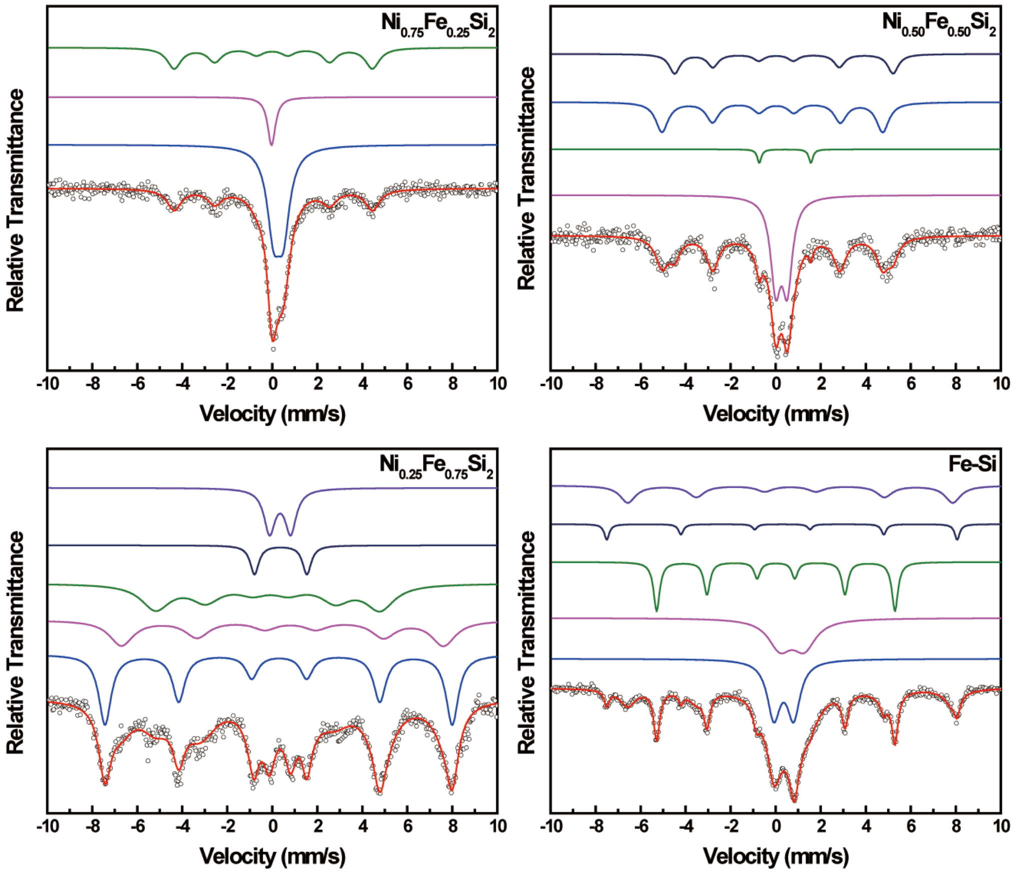

Figure 15. ^{57}Fe Mössbauer spectra of Fe substituted Ni-Si intermetallics.

for FeSi and ferrosilite ($FeSiO_3$) and two sextets for $FeNi_3$ and $Fe_{0.64}Ni_{0.36}$. The doublet with IS = 0.42 mm/s and QS = 2.49 mm/s can be assigned to trace $FeSiO_3$ (only accounted for 2.6%) [66, 67]. The formation of ferrosilite in the Fe substituted Ni-Si intermetallics can be attributed to the uncompleted silicification of iron oxides or the oxidation of the formed iron silicide. Due to the Fe:Ni molar ratio increasing, the account of Ni-rich Fe-Ni alloy decrease to 20.0%, while the Fe-rich Fe-Ni alloy ($Fe_{0.64}Ni_{0.36}$) with the account for 35.7% is appeared, which has the ^{57}Fe Mössbauer parameters of IS = -0.06 mm/s, QS = -0.08 mm/s, and H = 30.4 T.

For the $Ni_{0.25}Fe_{0.75}Si_2$ sample, the Mössbauer spectrum could be fitted with three sextets and two doublets. One sextuplet associated with $Fe_{0.64}Ni_{0.36}$ accounted for 28.4% of the total spectral area, while the two sextuplets with IS = 0.29 mm/s, QS = -0.03 mm/s, and H = 47.8 T and IS = 0.63 mm/s, QS = -0.35 mm/s, and H = 44.4 T are assigned to the two types of FeNi, respectively. In addition, two resolved doublets can be easily indentified, one attributed to $FeSiO_3$ and the other to Fe_2O_3. The present of Fe_2O_3 can be attributed that the zero-valent Fe is hardly silicided due to the content of Ni as catalyst decreasing, but oxidized by air during the passivation. This result is similar with the XRD result.

When the bulk Fe treated in SiH_4/H_2 at 450 ^{o}C to form Fe-Si, the Mössbauer spectrum could also be fitted into two doublets and three sextuplets. The sextuplet with IS = 0.01 mm/s, QS = 0 mm/s could be attributed to Fe^{o}, which accounted for 22.4% of the total spectral area. The other two sextuplets can be identified to Fe^{3+} in the tetrahedral site of spinel magnetite and the Fe irons located in the octahedral site [68]. The value of the mean isomer shift and hyperfine fields are similar to the bulk Fe_3O_4, which due to the partial oxidation of Zero-valent Fe [31]. The two doublets could again be ascribed to Fe_2O_3 and Si doped Fe_2O_3, respectively. The doublet with IS = 0.73 mm/s and QS = 1.08 mm/s is consistent with the reported Fe^{3+} value at six-coordinated sites in silicates and oxides [69]. During the silicifiaction process, the Si atoms are doped into the lattice of Fe_2O_3 and formed Fe-Si-O bond.

Table 5. ^{57}Fe Mössbauer parameters of the Fe substituted Ni-Si intermetallics.

Sample	Iron sites	IS/mm/s	QS/mm/s	H/T	RI/%	LW/mm/s
$Ni_{0.75}Fe_{0.25}Si_2$	FeSi	0.27	0.43	-	56.4	0.70
	$FeSi_2$, Cubic	-0.03	-	-	10.5	0.42
	$FeNi_3$	0.02	0.05	27.3	33.1	0.77
$Ni_{0.50}Fe_{0.50}Si_2$	$Fe_{0.64}Ni_{0.36}$	-0.06	-0.18	30.4	35.7	0.68
	FeSi	0.26	0.52	-	41.7	0.55
	$FeSiO_3$	0.42	2.29	-	2.6	0.22
	$FeNi_3$	0.19	0.34	30.1	20.0	0.59
$Ni_{0.25}Fe_{0.75}Si_2$	FeNi, Taemite	0.29	-0.03	47.8	33.6	0.66
	FeNi, Kamacite	0.63	-0.35	44.4	23.6	1.30
	$Fe_{0.64}Ni_{0.36}$	-0.14	-0.12	30.9	28.4	1.56
	$FeSiO_3$	0.37	2.33	-	4.9	0.46
	Fe_2O_3	0.35	0.93	-	9.5	0.61
Fe-Si	Fe_2O_3	0.36	0.88	-	27.5	0.71
	Si doped Fe_2O_3	0.73	1.08	-	24.5	1.25
	Fe^{o}	0.01	-0.01	32.8	22.4	0.33
	Fe_3O_4 A_{Tet}	0.29	-0.02	48.3	5.8	0.27
	Fe_3O_4 B_{Oct}	0.65	0	44.8	19.9	0.85

Isomer shift (IS) is refered to α-Fe foil at room temperature. Uncertainty is ±5% of the reported value.

5.2. Dibenzothiophene hydrodesulfurization over Fe substituted Ni-Si intermetallics

The catalytic properties of Fe substituted Ni-Si intermetallics have been tested in the dibenzothiophene (DBT) hydrodesulfurization (HDS). The DBT HDS activities of the Fe substituted Ni-Si intermetallics catalysts are plotted as a function of the Ni metal fraction (Ni/(Ni+Fe)) in Figure 16a. Stating from the Fe-Si catalyst, the HDS activities are low up to the $Ni_{0.50}Fe_{0.50}Si_2$ catalyst, but beyond this composition, the activity increases as the catalyst become Ni-rich $Ni_{0.75}Fe_{0.25}Si_2$ catalyst, which had an activity (48.7 nmol/g/s) higher than that of $NiSi_2$ catalyst (32.9 nmol/g/s). The DBT HDS results are consistent with those reported previously for $Ni_xCo_{1-x}Si_2$ catalysts [19]. A Fe-Si catalyst had a very low DBT HDS activity (as did a $CoSi_2$ catalyst), but the substitution of a small amount of Fe (or Co) into nickel silicide yielded catalysts ($Ni_{0.75}Fe_{0.25}Si_2$ and $Ni_{0.75}Co_{0.25}Si_2$) that had DBT HDS activities (40-50%) higher than that of a $NiSi_2$ catalyst. These results indicated that new sites were created, probably by the positive synergistic effect on HDS activity due to the addition of a second metal to nickel silicide, which are consistent with those studies by Smith and Bussell, who observed that unsupported $Co_{0.08}Ni_2P$ and $Fe_{0.03}Ni_{1.97}P_2$ catalysts had significantly higher activity than that of a Ni_2P catalyst for HDS of DBT [70, 71]. Based on the Mössbauer spectroscopy results for the iron-containing catalysts, the high HDS activity can be correlated to the modified nickel sites in the $NiSi_2$ due to the formation of Ni-Fe and Fe-Si bonds. An increase in the valence electron concentration through the Fe substitution weakens the Si–Si interactions but enhances the metal-silicon and metal-metal interactions, which may enhance the π adsorption of DBT, promoting the hydrogenation activity [72]. The selectivity results at steady state also showed remarkable dependency on compositions. As the formation of Fe substituted Ni-Si intermetallics, the product selectivity for Ni-rich $Ni_{0.75}Fe_{0.25}Si_2$ catalysts shows preference for biphenyl (82.0%), but to a less extent than that observed for the Fe-Si (88.7%) and $NiSi_2$ (91.8%) catalysts. The substitution of Fe for Ni decreases the selectivity for the direct desulfurization (DDS) route, but greatly increases the selectivity for the hydrogenation pathway (HYD). This result can be associated with the formation of FeNi bimetallic alloys, which have been previously described and demonstrated improved catalytic hydrogenation performances with respect to pure Ni or Fe based catalysts [73, 74] .

As shown in the Figure 16b, the conversion of DBT over Fe substituted Ni-Si intermetallic catalysts increases with the increase of contact time in the HDS of DBT at 3 MPa H_2 and 340 °C. Typically, HDS conversion reaches 32.5% over $Ni_{0.75}Fe_{0.25}Si_2$ catalyst at the low contact time (1.26 min) and 75.8% at the high contact time (7.58 min). Among five catalysts, the nickel-rich $Ni_{0.75}Fe_{0.25}Si_2$ catalyst with the major phase $NiSi_2$ and FeNi alloy shows the highest conversion. Combined with the phase state analysis resultsof XRD and Mössbauer spectra, it can be ascertained that the formation of FeNi bimetallic alloy in the Fe substituted Ni-Si intermetallic dramatically promoted the HDS activity due to the alteration of the

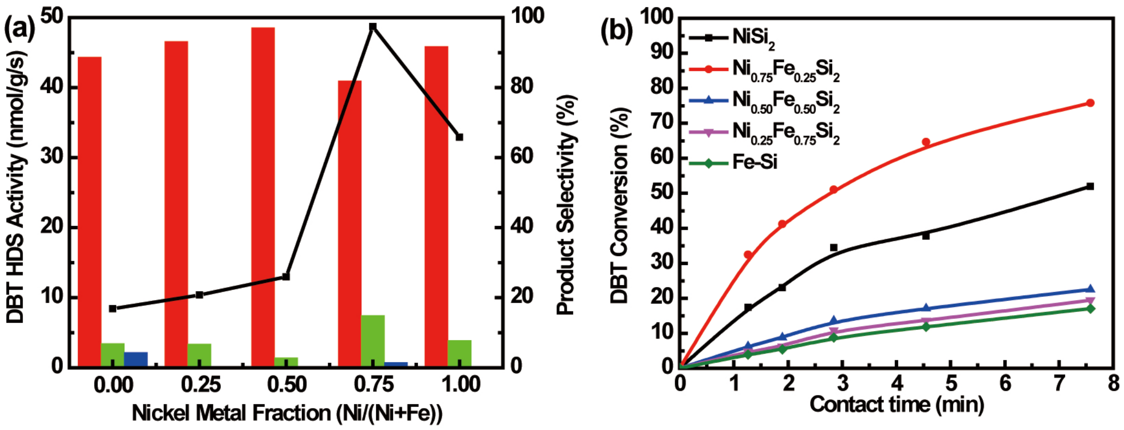

Figure 16. a) DBT HDS activity and product selectivity versus nominal Ni metal fraction for $Ni_{1-x}Fe_xSi_2$ catalysts. The reaction product to the red, green, and blue column is assigned to biphenyl, cyclohexylbenzene, and bicyclohexyl, respectively. b) Conversion of DBT versus the contact time at 3 MPa H_2 and 340 °C over Fe substituted Ni-Si intermetallics.

electronic structure by the chemical bonding between Ni and Fe. In the Fe substituted Ni-Si intermetallics, the Ni and Fe sites possess small positive charges. The DFT calculations have shown that the replacement of Ni atoms in $NiSi_2$ with Fe atoms (with higher d-electron counts) increases the d electron density of metal near the Fermi level because of an electron transfer from Ni to Fe [75]. As proposed by Ueckert et al., the metal site with a high electron density favors the formation of the π back bond between the aromatic ring and metal sites, which promotes the hydrogenation of the aromatic ring [76]. This may be one reason for the higher activity of the Ni-rich nickel iron bimetallic silicides.

6. Conclusion

This review covers Mössbauer spectroscopic studies of Fe-based silicides nanoparticles performed by our group. Using various synthesis methods, such as mechanical alloying, pyrolysis of silicon-containing metallic precursor, and temperature programmed silicification, we prepared the bulk and supported Fe-based silicides controllably from macroscopic scale to molecular level. These methods can also be derived to synthesis bimetallic silicides nanoparticles. Mössbauer spectroscopy has matured into one of the classical techniques for Fe-based silicides characterization. The technique is used to identify phases and provide information on the structure of silicides. In addition, Mössbauer spectra of iron silicides particles in applied magnetic fields can be used to determine particles sizes. ^{57}Fe Mössbauer spectroscopic results provided strong evidence the relationship between the structure of iron silicides and magnetic/catalytic properties.

Acknowledgement

We gratefully acknowledge financial support provided by the National Natural Science Foundation of China (21373038 and 21403026), the China Postdoctoral Science Foundation (2015T80255 and 2014M551068), and the Fundamental Research Funds for the Central Universities (DUT14RC(3)007).

References

[1] M. E. Schlesinger: Thermodynamics of solid transition-metal silicides, *Chem. Rev.*, **1990**, *90*, 607.

[2] A. L. Schmitt, J. M. Higgins , J. R. Szczech, S. Jin: Synthesis and applications of metal silicide nanowires, *J. Mater. Chem.*, **2010**, *20*, 223.

[3] A. Franciosi, J. H. Weaver, F. A. Schmidt: Electronic structure of nickel silicides Ni_2Si, NiSi, and $NiSi_2$, *Phys. Rev. B: Condens. Matter Mater. Phys.*, **1982**, *26*, 546.

[4] H. Thomas, I. I. Maugh: A new route to intermetallics metal silicides and related intermetallic compounds with unusual properties are formed by exposing supported metals to volatile organometallics, *Science*, **1984**, *225*, 403.

[5] W. P. Maszara: Fully silicided metal gates for high-performance CMOS technology: a review, *J. Electrochem. Soc.*, **2005**, *152*, G550.

[6] Y. Wu, J. Xiang, C. Yang, W. Lu, C. M. Lieber: Single-crystal metallic nanowires and metal/semiconductor nanowire heterostructures, *Nature*, **2004**, *430*, 61.

[7] Z. H. Liu, H. Zhang, L. Wang, D. R. Yang: Controlling the growth and field emission properties of silicide nanowire arrays by direct silicification of Ni foil, *Nanotechnology*, **2008**, *19*, 375602.

[8] N. Manyala, Y. Sidis, J. F. Ditusa, G. Aeppli, D. P. Young, Z. Fisk: Large anomalous Hall effect in a silicon-based magnetic semiconductor, *Nat. Mater.*, **2004**, *3*, 255.

[9] F. Zhou, J. Szczech, M. T. Pettes, A. L. Moore, S. Jin, L. Shi: Determination of transport properties in chromium disilicide nanowires via combined thermoelectric and structural characterizations, *Nano Lett.*, **2007**, *7*, 1649.

[10] H. T. Wang, J. C. Wu, Y. Q. Shen, G. P. Li, Z. Zhang, G. Z. Xing, D. L. Guo, D. D. Wang, Z. L. Dong, T. Wu: $CrSi_2$ hexagonal nanowebs, *J. Am. Chem. Soc.*, **2010**, *132*, 15875.

[11] Y. J. Lin, S. Zhou, X. H. Liu, S. Sheehan, D. W. Wang: $TiO_2/TiSi_2$ heterostructures for high-efficiency photoelectrochemical H_2O splitting, *J. Am. Chem. Soc.*, **2009**, *131*, 2772.

[12] A. Zhao, X. Zhang, X. Chen, J. Guan, C. Liang: Cobalt silicide nanoparticles in mesoporous silica as efficient naphthalene hydrogenation catalysts by chemical vapor deposition of $Co(SiCl_3)(CO)_4$ precursor, *J. Phys. Chem. C*, **2010**, *114*, 3962.

[13] X. Chen, A. Zhao, Z. Shao, C. Li, C. T. Williams, C. Liang: Synthesis and catalytic properties for phenylacetylene hydrogenation of silicide modified nickel catalysts, *J. Phys. Chem. C*, **2010**, *114*, 16525.

[14] X. Chen, M. Li, J. Guan, X. Wang, C. T. Williams, C. Liang: Nickel-silicon intermetallics with enhanced selectivity in hydrogenation reactions of cinnamaldehyde and phenylacetylene, *Ind. Eng. Chem. Res.*, **2012**, *51*, 3604

[15] X. Chen, J. Jin, G. Sha, C. Li, B. Zhang, D. Su, C. T. Williams, C. Liang: Silicon-nickel intermetallic compounds supported on silica as a highly efficient catalyst for CO methanation, *Catal. Sci. Technol.*, **2014**, *4*, 53.

[16] X. Chen, M. Zhang, K. Yang, C. T. Williams, C. Liang: Raney Ni-Si catalyst for selective hydrogenation of highly concentrated 2-butyne-1,4-

diol to 2-butene-1,4-diol in aqueous phase, *Catal. Lett.*, **2014**, *144*, 1118.

[17] L. Zhang, X. Chen, S. Jin, J. Guan, C. T. Williams, Z. Peng, C. Liang: Rapid microwaves synthesis of $CoSi_x$/CNTs as novel catalytic materials for hydrogenation of phthalic anhydride, *J. Solid State Chem.*, **2014**, *217*, 105.

[18] X. Chen, X. Liu, L. Wang, M. Li, C. T. Williams, C. Liang: High sulfur tolerance of Ni-Si intermetallics as hydrodesulfurization catalysts, *RSC Adv.*, **2013**, *3*, 1728.

[19] X. Chen, X. Wang, J. Xiu, C. T. Williams, C. Liang: Synthesis and characterization of ferromagnetic nickel-Cobalt silicide catalysts with good sulfur tolerance in hydrodesulfurization of dibenzothiophene, *J. Phys. Chem. C*, **2012**, *116*, 24968.

[20] S. Senthilarasu, R. Sathyamoorthy, S. Lalitha: Synthesis and characterization of β-$FeSi_2$ grown by thermal annealing of Fe/Si bilayers for photovoltaic applications, *Sol. Energy Mater. Sol. Cells*, **2004**, *82*, 299.

[21] K. S. K. Varadwaj, K. Seo, J. In, P. Mohanty, J. Park, B. Kim: Phase-controlled growth of metastable Fe_5Si_3 nanowires by a vapor transport method, *J. Am. Chem. Soc.*, **2007**, *129*, 8594.

[22] H. Okamoto, *Desk handbook: phase diagrams for binary alloys,* ASM International, Materials Park, OH, 2000.

[23] K. S. K. Varadwaj, K. Seo, J. In, P. Mohanty, J. Park, B. Kim: Phase-controlled growth of metastable Fe_5Si_3 nanowires by a vapor transport method, *J. Am. Chem. Soc.*, **2007**, *129*, 8594.

[24] J. R. Szczech, S. Jin: Epitaxially-hyperbranched FeSi nanowires exhibiting merohedral twinning, *J. Mater. Chem.*, **2010**, *20*, 1375.

[25] A. L. Schmitt, M. J. Bierman, D. Schmeisser, F. J. Himpsel, S. Jin: Synthesis and properties of single-crystal FeSi nanowires, *Nano Lett.*, **2006**, *6*, 1617.

[26] N. Dahal, V. Chikan: Phase-controlled synthesis of iron silicide (Fe_3Si and $FeSi_2$) nanoparticles in solution, *Chem. Mater.*, **2010**, *22*, 2892.

[27] X. Chen, B. Zhang, C. Li, Z. Shao, D. Su, C. T. Williams, C. Liang: Structural and electrochemical properties of nanostructured nickel silicides by reduction and silicification of high-surface-area nickel oxide, *Mater. Res. Bull.*, **2012**, *47*, 867.

[28] F. J. Berry, *Mössbauer spectroscopy applied to inorganic chemistry* Plenum Press: New York, 1984 Vol. 1. P 391

[29] K. Yang, X. Chen, J. Guan, C. Liang: Nickel silicides prepared from organometallic polymer as efficient catalyst towards hydrogenation of phenylacetylene, *Catal. Today*, **2015**, *246*, 176.

[30] J. Guan, X. Chen, K. Yang, A. Rykov, J. Wang, C. Liang: Preparation and size-dependent magnetism of highly dispersed iron silicide nanoparticles on silica, *J. Mater. Chem. C*, **2014,** *2*, 5292.

[31] M. Li, X. Chen, J. Guan, X. Wang, J. Wang, C. T. Williams, C. Liang: A facile and novel approach to magnetic Fe@SiO_2 and $FeSi_2$@SiO_2 nanoparticles, *J. Mater. Chem.*, **2012**, *22*, 609.

[32] M. Li, X. Chen, J. Guan, J. Wang, C. Liang: Thermally induced phase transition and magnetic properties of Fe-$FeSi_2$ with core-shell structure, *Phys. Status Solidi A*, **2013**, *210*, 2710.

[33] X. Chen, J. Guan, G. Sha, Z. Gao, C. T. Williams, C. Liang: Preparation and magnetic properties of single phase Ni_2Si by reverse Rochow reaction, *RSC Adv.*, **2014**, *4*, 653.

[34] D. Restrepo, S. M. Hick, C. Griebel, J. Alarcon, K. Giesler, Y. Chen, N. Orlovskaya, R. G. Blair: Size controlled mechanochemical synthesis of $ZrSi_2$, *Chem. Commun.*, **2013**, *49*, 707.

[35] B. Krumme, C. Weis, H. C. Herper, F. Stromberg, C. Antoniak, A. Warland, E. Schusyer, P. Srivastava, M. Walterfang, K. Fauth, J. Minár, H. Ebert, P. Entel, W. Keune, H. Wende: Local atomic order and element-specific magnetic moments of Fe_3Si thin films on MgO(001) and GaAs(001) substrates, *Phys. Rev. B*, **2009**, *80*, 144403.

[36] T. Shinjo, Y. Nakamura: Magnetic study of Fe_3Si and Fe_5Si_3 by mössbauer effect, *J. Phys. Soc. Jpn.*, **1963**, *18*, 797.

[37] G. K. Wertheim, J. H. Wernick, D. N. Buchanan: Mössbauer Effect in $Co_{1-x}Fe_xSi$, *J. Appl. Phys.* **1966**, *37*, 3333.

[38] M. A. Chuev: Multi-level relaxation model for describing the Mössbauer spectra of single-domain particles in the presence of quadrupolar hyperfine interaction, *J. Phys.: Condens. Matter*, **2011**, *23*, 426003-1.

[39] T. Li, Y. Z. Li, Y. H. Zhang: Phases in ball-milled, *J. Phys.: Condens. Matter*, **1997**, *9*, 1381.

[40] T. Sato, T. Iijima, M. Seki, N. Inagaki: Magnetic properties of ultrafine ferrite particles, *J. Magn. Magn. Mater.*, **1987**, *65*, 252.

[41] D. Nakagauchi, T. Yoshitake, K. Nagayama: Fabrication of ferromagnetic Fe_3Si thin films by pulsed laser deposition using an Fe_3Si target, *Vacuum*, ***2004***, *74*, 653.

[42] A. Ionescu, C. A. F. Vaz, T. Trypiniotis, C. M. Gürtler, H. García-Miquel, J. A. C. Bland, M. E. Vickers, R. M. Dalgliesh, S. Langridge, Y. Bugoslavsky, Y. Miyoshi, L. F. Cohen, K. R. A. Ziebeck: Structural, magnetic, electronic, and spin transport properties of epitaxial Fe_3Si/GaAs(001), *Phys. Rev. B*, **2005**, *71*, 094401-1.

[43] Q. Jiang, X. F. Cui, M. Zhao: Size effects on Curie temperature of ferroelectric particles, *Appl. Phys. A*, **2004**, *78*, 703.

[44] M. K. Kolel-Veetil, S. B. Qadri, M. Osofsky, R. Goswami, T. M. Keller: Carbon nanocapsule-

mediated formation of ferromagnetic Fe_5Si_3 nanoparticles, *J. Phys. Chem. C*, **2009**, *113*, 14663.

[45] M. Z. Wu, Y. D. Zhang, S. Hui, T. D. Xiao, S. H. Ge, W. A. Hines, J. I. Budnick and M. J. Yacaman: Magnetic properties of SiO_2-coated Fe nanoparticles, *J. Appl. Phys.*, **2002**, *92*, 6809.

[46] E. Murad, J. Cashion, *Mössbauer Spectroscopy of Environmental Materials and their industrial utilization*, Kluwer Academic Publishers: Boston, MA, 1984.

[47] K. Liu, A. Q. Wang, W. S. Zheng, J. H. Wang, Y. Q. Huang, J. Y. Shen, T. Zhang: Quasi in Situ 57Fe mössbauer spectroscopic study: quantitative correlation between Fe^{2+} and H_2 concentration for PROX over Ir−Fe/SiO_2 catalyst, *J. Phys. Chem. C*, **2010**, *114*, 8533.

[48] P. Schaaf, M. Milosavljevic, S. Dhar, N. Bibic, K. P. Lieb, M. Wölz, G. Principi: Mössbauer optimization of the direct synthesis of β-$FeSi_2$ by ion beam mixing of Fe/Si bilayers, *Hyperfine Interact.*, ***2002***, *139/140*, 615.

[49] H. Danan, A. Herr, A. J. P. Merer: New determinations of the saturation magnetization of nickel and iron, *J. Appl. Phys.*, **1968**, *39*, 669.

[50] S. W. Hung, P. H. Yeh, L. W. Chun, C. D. Chen, L. J. Chou, Y. J. Wu, L. J. Chen: Direct growth of β-$FeSi_2$ nanowires with infrared emission, ferromagnetism at room temperature and high magnetoresistance via a spontaneous chemical reaction method, *J. Mater. Chem.*, **2011**, *21*, 5704.

[51] E. Arushanov, M. Respaud, J. M. Broto, Ch. Kloc, J. Leotin, E. Bucher: Magnetic properties of β-$FeSi_2$ single crystals, *Phys. Rev. B: Condens. Matter.*, **1996**, **53**, 5108.

[52] E. Arushanov, G. Behr, J. Schumann: Magnetic properties of β-$FeSi_2$ single crystals, *Thin Solid Films*, **2004**, *461*, 148.

[53] S. Kondo, K. Yamada: On the appearance of induced magnetic moment of β-$FeSi_2$ by doping halogen or oxygen atoms, *Thin Solid Films*, **2004**, *461*, 193.

[54] O. Valassiades, C. A. Dimitriadis, J. H. Werner: Galvanomagnetic behavior of semiconducting $FeSi_2$ films, *J. Appl. Phys.*, **1991**, *70*, 890.

[55] M. Fanciulli, C. Rosenblad, G. Weyer, A. Svane, N. E. Christensen, H. von Känel: Conversion electron Mössbauer spectroscopy study of epitaxial β-$FeSi_2$ grown by molecular beam epitaxy, *Phys. Rev. Lett.*, **1995**, *75*, 1642.

[56]H.H. Hamdeh, M.M. Eltabey, J.C. Ho, P.C. Lee, K. Chen, Y.Y. Chen: Magnetism in nanoparticles of semiconducting $FeSi_2$, *J. Magn. Magn. Mater.*, **2010**, *322*, 2227.

[57] F.T. Lin, D.M. Jiang, X.M. Ma, W.Z. Shi: Structural order and magnetic properties of Fe_3Si/Si (100) heterostructures grown by pulsed-laser deposition, *Thin Solid Films*, **2007**, *515*, 5353.

[58] M.B. Stearns: Internal magnetic fields, isomer shifts, and relative abundances of the various Fe sites in FeSi alloys, *Phys. Rev.*, **1963**, *129*, 1136.

[59]R.M. Walser, R.W. Bene: First phase nucleation in silicon-transition metal planar interfaces, *Appl. Phys. Lett.*, **1976**, *28*, 624.

[60]V.A. Du, A. Sidorenko, O. Bethge, S. Paschen, E. Bertagnolli, U. Schubert: Iron silicide nanoparticles in a SiC/C matrix from organometallic polymers: characterization and magnetic properties, *J. Mater. Chem.*, **2011**, *21*, 12232.

[61] M. Rebhan, M. Rohwerder, M. Stratmann: CVD of silicon and silicides on iron, *Appl. Surf. Sci.*, **1999**, *140*, 99.

[62] G. A. Landrum, R. Hoffmann, J. Evers, H. Boysen: The TiNiSi family of compounds: structure and bonding, *Inorg. Chem.* **1998**, *37*, 5754.

[63] T. E. Cranshaw, C. E. Johnson, M. S. Ridout: The Mössbauer and NMR spectra of FeSi alloys, *Phys. Lett.* **1966**, *21*, 481.

[64] B. H. Zeifert, J. Salmones, J. A. Hernández, R. Reynoso, N. Nava, E. Reguera, J. G. Cabañas-Moreno, G. Aguilar-Ríos: X-Ray Diffraction and Mössbauer characterization of Raney Fe-Ni catalysts, *J. Radioanal. Nucl. Chem.* **2000**, *245*, 637.

[65] M. Vondráček, V. Dudr, N. Tsud, P. Lejček, V. Cháb, K.C. Prince, V. Matolín, O. Schneeweiss: Surface segregation in FeSi alloys, *Surf. Sci.*, **2006**, *600*, 4108.

[66] Y. A. Abdu, T. Ericsson: Mössbauer spectroscopy, x-ray diffraction, and electron microprobe analysis of the new haifa meteorite, *Meteoritics Planet. Sci.*, **1997**, *32*, 373.

[67] A. H. Cuttler: The behaviour of a synthetic ^{57}Fe doped kaolin: Mössbauer and electron paramagnetic resonance studies, *Clay Miner.* **1980**, *15*, 429.

[68] A. Mitra, J. Mohapatra, S. S. Meena, C. V. Tomy, M. Aslam Verwey: Transition in ultrasmall-sized octahedral Fe_3O_4 nanoparticles, *J. Phys. Chem. C*, **2014**, *118*, 19356.

[69] S. S. Hafner, H. G. Huckenholz: Mössbauer spectrum of synthetic ferri-diopside, *Nature*, **1971**, *233*, 9.

[70] A. F. Gaudette, A. W. Burns, J. R. Hayes, M. C. Smith, R. H. Bowker, T. Seda, M. E. Bussell: Mössbauer spectroscopy investigation and hydrodesulfurization properties of iron–nickel phosphide catalysts, *J. Catal.* **2010**, *272*, 18.

[71] I. I. Abu, K. J. Smith: The effect of cobalt addition to bulk MoP and Ni_2P catalysts for the hydrodesulfurization of 4, 6-dimethyldibenzothiophene, *J. Catal.* **2006**, *241*, 356.

[72] J. Yao, P. Lyutyy, Y. Mozharivskyj: Crystal structure, coloring problem and magnetism of $Gd_{5-x}Zr_xSi_4$, *Dalton.Trans.* **2011**, *40*, 4275.

[73] P. Gallezot, P. J. Cerino, B. Blanc, G. Flèche,

P. Fuertes: Glucose hydrogenation on promoted raney-nickel catalysts, *J. Catal.* **1994**, *146*, 93.

[74] S. Sitthisa, W. An, D. E. Resasco: Selective conversion of furfural to methylfuran over silica-supported NiFe bimetallic catalysts, *J. Catal.* **2011**, *284*, 90.

[75] J. A. Rodriguez, J. Y. Kim, J. C. Hanson, S. J. Sawhill, M. E. Bussell: Physical and chemical properties of MoP, Ni_2P, and MoNiP hydrodesulfurization catalysts: time-resolved X-ray diffraction, density functional, and hydrodesulfurization activity studies, *J. Phys. Chem. B*, **2003**, *107*, 6276.

[76] T. Ueckert, R. Lamber, N. I. Jaeger, U. Schubert: Strong metal support interactions in a Ni/SiO_2 catalyst prepared via sol-gel synthesis, *Appl. Catal., A*, **1997**, *155*, 75.